Mesoscopic structure of neuronal tracts from time-dependent diffusion

Lauren M. Burcaw, **Els Fieremans**, and **Dmitry S. Novikov**[*]

Bernard and Irene Schwartz Center for Biomedical Imaging, Department of Radiology, New York University School of Medicine, New York, NY 10016, USA

Abstract

Interpreting brain diffusion MRI measurements in terms of neuronal structure at a micrometer level is an exciting unresolved problem. Here we consider diffusion transverse to a bundle of fibers, and show theoretically, as well as using Monte Carlo simulations and measurements in a phantom made of parallel fibers mimicking axons, that the time dependent diffusion coefficient approaches its macroscopic limit slowly, in a $(\ln t)/t$ fashion. The logarithmic singularity arises due to short range disorder in the fiber packing. We identify short range disorder in axonal fibers based on histological data from the splenium, and argue that the time dependent contribution to the overall diffusion coefficient from the extra-axonal water dominates that of the intra-axonal water. This dominance may explain the bias in measuring axon diameters in clinical settings. The short range disorder is also reflected in the linear frequency dependence of the diffusion coefficient measured with oscillating gradients, in agreement with recent experiments. Our results relate the measured diffusion to the mesoscopic structure of neuronal tissue, uncovering the sensitivity of diffusion metrics to axonal arrangement within a fiber tract, and providing an alternative interpretation of axonal diameter mapping techniques.

Keywords

Diffusion; MRI; Time dependence; White matter; Microstructure; Axonal diameters

Introduction and overview of results

Diffusion-weighted magnetic resonance imaging (dMRI) has become a powerful tool for imaging the central nervous system, particularly with the advent of diffusion tensor imaging (Basser et al., 1994). Due to the directional and microstructural sensitivity of the diffusion-weighted signal (which has a meaning of the diffusion propagator), dMRI has become an indispensable tool for studying white matter (Beaulieu, 2002).

The diffusion propagator depends separately on the molecular displacement δx via the spatial Fourier wave vector q, and on the diffusion time t, Fig. 1. So far, the brain dMRI development has mainly focused on exploring as much of the q-space as is possible given

[*] Corresponding author. dima@alum.mit.edu (D.S. Novikov)..

clinical limitations, under the overarching theme of *q*-space imaging (Callaghan et al., 1988). This corresponds to proceeding vertically in Fig. 1, with diffusion time fixed at *t* ~50–100 ms in the clinical settings.

Here we explore the horizontal direction in Fig. 1, along the *t*-axis. We focus on the origin of the time dependence of mean squared displacement $\langle[\delta x(t)]^2\rangle$ of water molecules, characterized by the diffusion coefficient $D(t) = \langle[\delta x(t)]^2\rangle/2t$.

As axonal walls are believed to be the major restrictions to diffusion in the white matter (Beaulieu, 2002), the biophysical challenge is to identify which μm-level features of axonal packing within a fiber tract are most pronounced in a dMRI measurement with a macroscopic, mm-level resolution. It turns out that the relative importance of different features of axonal geometry depends on the measurement time scales.

Early understanding of $D(t)$ has relied on the result of Mitra et al. (1992), who found that the initial decrease of $D(t)$ is determined solely by the net surface area of all barriers, such as cell walls, irrespective of their positions. With transverse dimensions of axons and dendrites of ~1 μm (Lamantia and Rakic, 1990), and water diffusion coefficient ~1 μm²/ms, this limit demands time scales below 1 ms. These are unrealistically short for the human brain dMRI.

Fortunately, the time dependence observed in neuronal tissue (Horsfield et al., 1994; Does et al., 2003; Assaf et al., 2008; Alexander et al., 2010; Aggarwal et al., 2012; Portnoy et al., 2013; Kunz et al., 2013; Pyatigorskaya et al., 2013; Kershaw et al., 2013; Baron and Beaulieu, 2013; Van et al., 2014; Burcaw et al., 2014) extends onto feasible times *t* ~1–10 ms and even beyond, which prompts us to explore the long time limit of $D(t)$, and its connection to axonal tract geometry. This is the main objective of this work.

For *t* long enough so that water molecules travel past one or more axons, it is not just the net amount of the restrictions, such as axonal membranes and myelin, but the correlations in their positions and orientations that determine the diffusion propagator (Novikov and Kiselev, 2010) and the derived diffusion metrics (Szafer et al., 1995; Fieremans et al., 2008; Novikov and Fieremans, 2012; Fieremans et al., 2012) . In particular, when $D(t)$ is approaching its macroscopic $t \to \infty$ (tortuosity) asymptote D_∞, the short-distance details become irrelevant, while the behavior of $D(t)$ is determined by how spatially correlated are the restrictions at large distances (Novikov et al., 2014). These correlations are characterized by the structural exponent *p*, cf. Theory section.

In this work, we apply the framework (Novikov et al., 2014) to diffusion in the extra-axonal space at experimentally feasible diffusion times, and obtain the following four results:

(i)   By analyzing histology data, we identify the short range disorder in the two-dimensional fiber tract cross-section (exponent *p* = 0), and determine how this randomness in fiber packing manifests itself in the long-time behavior of the common diffusion metrics. These results, summarized in Table 1, are independent of whether axonal walls are permeable or not.

(ii)   By performing time-dependent pulsed-gradient (PG) DTI on a fiber phantom designed to mimic the diffusion in the extra-axonal space, as well as using

Monte Carlo simulations, we confirm the logarithmic singularity in $D(t)$, cf. Table 1:

$$D\left(t\right) \simeq D_\infty + A \cdot \frac{ln\left(t/\tilde{t}_c\right)}{t}, \quad t \gg \tilde{t}_c \sim max\left\{t_c, \delta\right\}. \quad (1)$$

Here the coefficient A is proportional to the value $\Gamma(k)|_{k \to +0}$ of the power spectrum of fibers within the two-dimensional (2d) cross-section [cf. Appendix A, Eq. (A.4)], and t_c represents the time to diffuse across the correlation length l_c of the 2d random packing geometry. For realistic axonal packings, l_c closely follows mean external axonal radius, with t_c 1 ms for the brain, while A roughly scales with l_c^2, Table 2. The $(\ln t)/t$ singularity occurs due to the short range 2d disorder in fiber packing (exponent $p = 0$), and is absent in an ordered (lattice) arrangement ($p = \infty$), as our simulations demonstrate. For PG with pulse width $\delta > t_c$, $\ln(t/t_c)$ in Eq. (1) crosses over to $\ln(t/\delta)$, $t \gg \delta$.

(iii) Equivalently, the 2d short-range disorder leads to the character istic $\sim |\omega|$ frequency dependence, cf. Table 1,

$$Re\mathscr{D}\left(\omega\right) \simeq D_\infty + A \cdot \frac{\pi}{2}|\omega|, \quad |\omega|t_c \ll 1 \quad (2)$$

of the oscillating gradient (OG) measured diffusion coefficient $D(\omega)$ transverse to axons. By virtue of the cumulant expansion (Kiselev, 2010), Eq. (1) or (2) allows one to calculate the effect of the disordered fiber geometry on any gradient wave form. We show that recent OG ex vivo data (Portnoy et al., 2013) exhibit the behavior (Eq. (2)). This confirms our conclusion about the short range disorder, $p = 0$, in fiber packing. Hence, the structural disorder renders OG measurements insensitive to intra-axonal water at low ω, as the latter contributes a less pronounced, quadratic frequency dependence $\sim \omega^2 \ll |\omega|$ for $\omega \to 0$.

(iv) The singularity (Eq. (1)) provides a different interpretation of ax onal diameter mapping results. Under a common assumption of no exchange between compartments, we argue that the contri bution (Eq. (1)) is more relevant (decays slower) than the $1/t$ contribution from water confined inside axons. Hence, structural disorder in axonal packing amplifies the role of extra-axonal water. This may explain (Fig. 2 and Table 3) the well-known overestimation of axon diameters, by factors of ~3–5 or even more, in clinical dMRI (Alexander et al., 2010; Zhang et al., 2011). This bias has been previously attributed to the insensitiv ity of the AxCaliber (Assaf et al., 2008) scheme to small axons (Dyrby et al., 2012) or to the noise. We believe the reason may be more fundamental: for quantifying compartment sizes and the residual time-dependent (and hence non-Gaussian) nature of diffusion in the extracellular space should not be neglected. This is especially relevant for clinical dMRI, when the extra-axonal signal is dominated by its first few cumulants.

The outline of this paper is as follows. Theoretical arguments in favor of results (i)–(iii) and Eqs. (1)–(2), as well as establishing $p = 0$ for a fiber tract, are given in Theory section. After

we present our methods, the experimental and numerical validation of (ii) and (iii) and their im plications for OG and PG measurements are given in Results section. Our new interpretation (iv) of axonal diameter mapping, the phase diagram for PG measurements transverse to axons (Fig. 12), and the explanation of how Fig. 2 has been obtained, are outlined in Discussion section.

Theory

One of the fundamental questions of brain dMRI is to identify relevant μm-level structural features that affect the observed signal the most. Addressing it would help develop parsimonious models of diffusion in neuronal tissue in order to become specific to pathological changes at the earliest stages of disease.

Here we identify and quantify the effect of the randomness (disorder) in packing of neuronal fibers in a bundle (Fig. 3) as the relevant structural characteristic observable in brain dMRI, especially at the clinically feasible diffusion times. Our main object of investigation will be the power spectrum $\Gamma(k)$ of the restrictions, Fig. 4, which is the Fourier transform of their density correlation function $\Gamma(r)$ (cf. Appendix B). We will demonstrate that the way nature packs axons within a bundle, Figs. 3e–f, is qualitatively similar to the random packings produced in Figs. 3b–d — in all cases, the packings are of the so-called short-range disorder type. The similarity in the structure will lead to similarly behaving diffusion metrics and to the qualitative differences from those in the ordered packing of Fig. 3a and Table 1.

Relation of time dependent diffusion to structural correlations

The PG diffusion weighting in the narrow-pulse limit yields the time-dependent diffusion coefficient, commonly defined as (Callaghan, 1991)

$$D(t) = \frac{\left\langle [\delta x(t)]^2 \right\rangle}{2t}, \quad t \geq 0, \quad (3)$$

where $\delta x = x(t) - x(0)$ is the displacement in a chosen direction $\hat{x}$ along the Brownian path $r(t)$. For the purpose of investigating the temporal evolution, we find it useful to define the instantaneous diffusion coefficient via a time derivative,

$$D_{inst}(t) \equiv \frac{\partial}{\partial t} \frac{\left\langle [\delta x(t)]^2 \right\rangle}{2} = \frac{\partial}{\partial t}[tD(t)], \quad t \geq 0. \quad (4)$$

While the PG diffusion coefficient (Eq. (3)) characterizes the average rate of the evolution of the mean squared displacement over the whole measurement interval t and is a cumulative quantity, the instantaneous one describes its rate of change at the moment t. In uniform fluids, $D \equiv D_{inst} = $ const. In heterogeneous media such as tissues, it is $D_{inst}(t)$ that is most directly related to structure probed at the current diffusion length scale $L(t) = \sqrt{\left\langle [\delta x(t)]^2 \right\rangle}$.

Definitions of Eqs. (3) and (4) assume the narrow-pulse limit, where the pulse width δ is smaller than any characteristic time scale. For understanding the physics of diffusion in restricted geometry, these fundamental metrics are the most transparent ones to consider; the effects of finite δ will be derived from them below.

At long t, the way of approaching the macroscopic limit D_∞

$$D_{inst}(t) \simeq D_\infty + const \cdot t^{-\vartheta}, \quad t \to \infty \quad (5)$$

is characterized by a dynamical exponent ϑ whose value is directly connected to the structure via (Novikov et al., 2014)

$$\vartheta = (p+d)/2 \quad (6)$$

in d spatial dimensions, generalizing earlier approaches (Ernst et al., 1984; Machta et al., 1984; Visscher, 1984). The structural exponent p determines the character of the long-range spatial correlations of the re strictions, via the low-k behavior of their power spectrum (Appendix B)

$$\Gamma(k) \sim k^p, \quad k \to 0. \quad (7)$$

The relations of Eqs. (5) and (6) enable grouping differently looking media (tissues) into a relatively few distinct structural universality classes defined in terms of their structural exponent p. In other words, the dynamics of the observable diffusion coefficient is qualitatively similar for all d-dimensional media with the same structural exponent p describing the long-range ($k \to 0$) behavior (Eq. (7)) of the power spectrum of the restrictions (Novikov et al., 2014).

Here we consider the two most common classes, short range disor der ($p = 0$) and order ($p = \infty$). We will show that the former corre sponds to neuronal tissue, and use the comparison with the latter to exemplify the role of the structural disorder. Other disorder universality classes (Novikov et al., 2014) are characterized by distinct values of the exponent p in Eq. (7).

Fig. 4 shows the 2d angular-averaged density power spectrum, or equivalently, the spatial Fourier transform $\Gamma(k)$, Eq. (B.2), of the density correlators (Eq. (B.1)), for our examples from Fig. 3 (see Appendix B for details). We observe that the low-k behavior, which reflects the long range correlations, is qualitatively similar for the disordered arrangements of Fig. 3, Panels b–d, and distinctly different in the periodic (ordered) case of Fig. 3a.

Short range disorder is characterized by a finite plateau $\Gamma(k)|_{k \to +0} > 0$. It corresponds to exponent $p = 0$ in Eq. (7), and reflects the absence of long range correlations at distances beyond the disorder correlation length $l_c \sim 1/k_c$, where k_c is of the order of the extent of the low-k plateau (i.e. $\Gamma(r)$ is a peak of the width $\sim l_c$). This is the most prevalent disorder class, qualitatively similar to Poissonian disorder (for which there are no spatial correlations, e.g. for the centers of the disks in Fig. 3d).

For the opposite case of ordered arrangement, Fig. 3a, $\Gamma(k)$ is a set of δ-function peaks at the reciprocal lattice vectors k_n, so that $\Gamma(k)\equiv 0$ when k is within a circle of radius less than the distance to the smallest recip rocal lattice vector k_0. While this $\Gamma(k)$ does not possess axial symmetry, we can still consider the angular-averaged $\Gamma(k)$ so as to compare with the disordered cases above. This $\Gamma(k)$ vanishes identically, $\Gamma(k)\equiv 0$, for $k < k_0$. In the case of Fig. 3, $k_0 = \pi/l_0$, where l_0 is the lattice constant (shortest distance between disk centers). From the point of the general classification (Novikov et al., 2014), this means that $\Gamma|_{k<k0}$ is smaller than any power law k^p with arbitrary large p as $k \to 0$, hence formally $p = \infty$ for any perfect lattice.

The relations of Eqs. (5) and (6) now predict qualitatively different behavior for $D_{\mathrm{inst}}(t)$. The short range disorder in Figs. 3b–d yields the exponent $\vartheta = 1$ in $d = 2$ dimensions, resulting in

$$p=0 : D_{inst}(t) \simeq D_\infty + \frac{A}{t}, \quad t \gg t_c, \quad (8)$$

where t_c is the time to diffuse across the disorder correlation length l_c (in our examples, l_c is of the order of the disk size).

In Appendix A we show that the coefficient A is proportional to the plateau value $\Gamma(k)|_{k \to +0}$ in Fig. 4. Roughly speaking, the value of A reflects the "strength" of the short range disorder component, and determines how pronounced is the power law tail (Eq. (8)).

On the other hand, $D_{\mathrm{inst}}(t)$ in an ordered medium approaches its macroscopic limit exponentially fast, as there is no plateau, $\Gamma(k)|_{k<k0}\equiv 0$, and thus no power law, $A\equiv 0$:

$$p=\infty : D_{inst}(t) \simeq D_\infty + const \cdot e^{-t/t_0}, \quad t \gg t_0. \quad (9)$$

The exponential approach of D_∞ is faster than any inverse power law $t^{-\vartheta}$. This allows us, using the nomenclature of Novikov et al. (2014), to formally assign the dynamical exponent $\vartheta = \infty$ to any lattice; this value of ϑ is then in agreement with Eq. (6) for $p = \infty$. Qualitatively, one can view any lattice as a limiting case of a so-called hyperuniform arrange ment (Torquato and Stillinger, 2003) (with infinitely small long-range fluctuations).

The fast decrease (Eq. (9)) in $D_{\mathrm{inst}}(t)$ occurs for times exceeding t_0, which is of the order of the diffusion time across the period l_0. Note that a similar, exponentially fast approach of the value $D_\infty = 0$ also occurs when random walkers are confined in an impermeable pore, cf. Appendix C, Eq. (C.5) and Fig. C.1, for an impermeable cylinder example.

As we can see, $D_{\mathrm{inst}}(t)$ can be used to probe long-range correlations in tissue architecture. Measurement of the exponent ϑ, with the knowledge of sample's dimensionality d, can allow one to identify whether the sample is ordered or disordered, and determine the disorder universal ity class. The latter can be also identified by determining the exponent p from histology. Below we determine p, as well as find out how ϑ can be identified in practically measurable PG and OG diffusivities.

Structural and dynamical exponents transverse to neuronal fibers

What is the structural exponent p for white matter? To answer this question, we obtain an electron microscope histology image of a mouse splenium (Zurek et al., 2014), shown in Fig. 3e, and identify myelinated axons as the restrictions for water molecules in the extra-axonal space. We then manually outline all axons, including both intra-axonal space and myelin, assign to them a unit density $\rho(r) = 1$, and generate an image shown in Fig. 3f, similar to those for the disk packings. The correlation analysis as described above now yields the finite plateau $\Gamma(k)_{k<k} \simeq \mathrm{const}<0$ in Fig. 4, corresponding to

$$p=0 \quad \text{transverse to white matter fibers} \quad (10)$$

and a very short disorder correlation length $l_c \sim 1/k_c \sim \langle r_{\text{ext}} \rangle$ 1μm. While the plateau in $\Gamma(k)$ is not fully pronounced due to a relatively small number of axons within the available histology slide, we believe that there is neither a tendency of ordering (which would result in the decrease of $\Gamma(k)$ as $k \to 0$), nor strong fluctuations (which would cause the divergence in $\Gamma(k)$ as $k \to 0$).

We note that p may seem slightly negative, which would indicate density fluctuations somewhat stronger than those of short-range disorder. We currently believe that this is most likely an artifact of a finite-size histology slide; indeed, the exponents p take well-defined discrete values, and we are not aware of a universality class with a negative p such that $|p| \ll 1$.

Interestingly, while the axonal volume fraction is 0.7, comparable to the disordered packing in Fig. 3b, the plateau for the axons occurs at a value similar to the $\varphi = 0.5$ disordered disk packing in Fig. 3c. This reflects fairly large heterogeneities in the axonal packing: note the presence of both highly dense axon clusters and voids in the histology tracing. Similar heterogeneities can be seen in the $\varphi = 0.5$ random disk packing.

To conclude, the analysis of the available histology is compatible with the short range disorder in the packing of neuronal fibers within a bundle.

The observation (Eq. (10)) has a number of consequences.

1. Short range disorder is the most common disorder type — nature did not surprise us here. We could have expected reduced spatial correlations, if evolution's goal were to pack axons most efficiently. That would have led to $p > 0$, similar to the exponent $p \approx 1$ for the "maximally random jammed" packing of spheres in $d = 3$ dimensions (Donev et al., 2005a). Conversely, axons do not look particularly "jammed".

2. The absence of very strong long-range correlations (which would be characterized by a strongly diverging $\Gamma(k)$ with $p < -d$) is consistent with having a finite nonzero macroscopic diffusion constant D_∞ transverse to the axons, and is incompatible with the so-called anomalous diffusion (Bouchaud and Georges, 1990) for which D_∞ does not exist. In other words, under the common assumption of cell walls providing the most important restrictions to diffusion, at distances beyond l_c the hindered extra-axonal diffusion should asymptotically become normal. Our histology-based evidence con tradicts the models of the

"anomalous", or "fractal" diffusion in the brain (continuous time random walks, stretched exponentials). Here we show that the Gaussian limit is approached slowly, so that the residual non-Gaussianity can matter at long but finite t. This slowness is a likely reason for relatively good fits provided by unphysical stretched-exponential models in a finite range of q and t.

3. Based on Eq. (6), we predict the dynamical exponent

$$\vartheta = 1 \quad \text{transverse to white matter fibers} \quad (11)$$

which will result in the behavior of Eqs. (1) and (2) as we discuss below. (In the unlikely case of p turning out to be small and negative as mentioned after Eq. (10), the corresponding $\vartheta < 1$ would make the time-dependence of diffusion in the extra-axonal space even more dominant than we anticipate.)

4. The exponent (Eq. (10)) gives us a practical recipe to represent and model the packing disorder in white matter. For instance, Monte Carlo simulations should be performed for the random packings rather than for the periodic ones, even at the cost of more challenging implementation. Below, we will identify the dynamical exponent (Eq. (11)) in the Monte Carlo data for diffusion transverse to simulated phantoms such as shown in Figs. 3b, and c.

5. The short range disorder identified in the white matter justifies building artificial diffusion phantoms in which the same disorder class occurs, e.g. due to random packing of hydrophobic fibers in a bundle. In what follows, we will describe how we identify the dynamical exponent $\vartheta = 1$, and thereby the structural exponent $p = 0$, in such a phantom.

Origin of the logarithmic singularity, Eq. (1)

While the power law dependence of $D_{\text{inst}}(t)$ reveals profound differences in the structure, a narrow-pulse PG MR measurement yields the cumulative diffusion coefficient (Eq. (3)), in which these differences may be masked. From Eq. (4),

$$D(t) = \frac{1}{t} \int_0^t D_{inst}\left(t'\right) dt'. \quad (12)$$

One can see that, whenever we are dealing with structures for which $D_{\text{inst}}(t) - D_\infty$ decreases faster than $1/t$, the corresponding difference $D(t) - D_\infty$ always behaves as $1/t$ at long t. This is because the integral in Eq. (12) converges as $t \to \infty$, and hence, to the leading approximation, it can be substituted by its $t = \infty$ limit, $\int^t \ldots \to \int^\infty \ldots = \text{const} < \infty$. Therefore, e.g. both for a periodic (ordered) medium, and for fully confining pores (cells), the cumulative diffusion coefficient

$$\vartheta > 1 : D(t) \simeq D_\infty + \frac{const}{t}, \quad t \gg t_0. \quad (13)$$

Overall, in all cases with the dynamical exponent $\vartheta > 1$, i.e. when $p > 2 - d$, $D(t)$ will behave in the same way, Eq. (13), which makes it practically harder to distinguish between media with different types of structural correlations using PG DTI.

The exponent $\vartheta = 1$, cf. Eq. (8), which is the subject of our focus, causes a logarithmic divergence $\int_{\tilde{t}_c}^{t} dt'/t' = ln\,(t/\tilde{t}_c)$ in Eq. (12). Hence, its presence survives, albeit marginally, the temporal averaging inher ent to the cumulative $D(t)$, and yields a logarithmically enhanced time dependence (Eq. (1)) as a function of the upper limit, t, relative to that in an ordered or confining geometry, Eq. (13). This is one of our main re sults (cf. Table 1) to be checked in simulations and experiment. The lower limit $\tilde{t}_c$ is the time scale beyond which the tail (Eq. (8)) entering Eq. (12) dominates; when PG pulse width $\delta \ll t_c$, $\tilde{t}_c = t_c$, while for $\delta \ll \tilde{t}_c \sim \delta$, as it will be derived in Eqs. (24) and (25) below.

To summarize, the logarithmic singularity (Eq. (1)) in $D(t)$ arises from averaging over time the slow $1/t$ tail in $D_{\text{inst}}(t)$ coming from the short range disorder in two spatial dimensions.

Implications for OG-measured D(ω), Eq. (2)

Practically, the long-time limit for neuronal tissue occurs already for relatively short times from the point of a conventional PG measurement. Hence, to increase the diffusion weighting and to access shorter time scales, it is convenient to utilize oscillating gradient methods (Does et al., 2003).

We begin with the relation [Eq. (8) of Novikov et al. (2014)]

$$\mathscr{D}(\omega) = -\,i\omega \int_0^\infty dt\, e^{i\omega t} D_{inst}(t) \quad (14)$$

between $D_{\text{inst}}(t)$ and the dispersive diffusivity defined via velocity autocorrelation function (Novikov and Kiselev, 2010)

$$\mathscr{D}(\omega) = \int_0^\infty \langle v(t)\, v(0)\rangle\, e^{i\omega t} dt. \quad (15)$$

Eq. (14) is a nonlocal in time relation between $D_{\text{inst}}(t)$ and $D\omega$, with these two quantities having identical information content. also note (Novikov and Kiselev, 2010, 2011) that the OG-measured frequency-dependent diffusivity

$$\frac{1}{2} \int_{-\infty}^\infty dt\, e^{i\omega t} \langle v(t)\, v(0)\rangle \equiv Re\, \mathscr{D}(\omega) \quad (16)$$

equals the real part of $D(\omega)$ defined in Eq. (15). Hence, the general relation between the OG measurement and $D_{\text{inst}}(t)$ is

$$OG\!:\!Re \quad \mathscr{D}(\omega) = \omega \int_0^\infty dt\, sin\,\omega t \quad D_{inst}(t). \quad (17)$$

Let us now focus on the low-frequency behavior of $D\omega$, corresponding to the $1/t$ tail (Eq. (8)). Using $\int_0^\infty dt\,(\sin\omega t)/t = (\pi/2)\,\text{sgn}\,\omega$, Eq. (17) yields the result (Eq. (2)) advertised in the Introduction section, which is the OG counterpart of Eqs. (1) and (8). Hence, the dynamical exponent $\vartheta = 1$ is reflected in the $1/t \leftrightarrow (\pi/2)|\omega|$ correspondence between the tails in $D_{\text{inst}}(t)$ and in Re $D(\omega)$. We also note that the $1/t$ tail in D_{inst} is equivalent to the tail

$$p{=}0: \langle v\left(t\right)v\left(0\right)\rangle \simeq -\frac{A}{t^2}, \quad t \gg t_c, \quad (18)$$

(Ernst et al., 1984) in the velocity autocorrelation function, in contrast to its exponentially fast decay $\sim -e^{-t=t0}$ for ordered ($p = \infty$) or confined geometries.

It is instractive to find the full $D(\omega)$, Eq. (14). Estimating

$$\int_{t_c}^{\infty}\frac{dt}{t}e^{i\omega t} \simeq \int_{t_c}^{-1/i\omega}\frac{dt}{t}{=}ln\frac{1}{-i\omega t_c}, |\omega|t_c \ll 1$$

with logarithmic accuracy (neglecting terms ~1 as compared to the large logarithm above), we choose t_c as the lowest limit of integration (time scale from which the tail begins), and $-1/i\omega$ as a long-time cutoff provided by the oscillating $e^{i\omega t}$. Thus

$$p{=}0: \mathscr{D}\left(\omega\right) \simeq D_{\infty}{+}A \cdot i\omega\,ln\left(-i\omega t_c\right), \quad |\omega|t_c \ll 1. \quad (19)$$

This of course agrees with the direct calculation of the integral in Eq. (A.1) with $\Gamma_D(k) \to$ const for k k_c. Taking the real part again yields Eq. (2), since $ln(-i) = -i\pi/2$, whereas the logarithmic singularity $ln\omega$ goes entirely into the unobservable (albeit recoverable using Kramers–Kronig dispersion relations) imaginary part Im $D(\omega){\simeq}A$ $\omega ln|\omega t_c|$, odd in ω, Fig. 5a.

The diffusivity (Eq. (19)) and its real part (Eq. (2)) are non-analytic in frequency around $\omega = 0$, Fig. 5. The physical origin of this behavior is the structural disorder that results in the finite density of disorder eigenstates (i.e. eigenstates of the Laplace equation with the stochastic $D(r)$). As it follows from Eq. (A.1) in Appendix A, this continuum of states, whose weight is determined by the disorder strength embodied in the coefficient A, Eq. (A. 4), contributes to the diffusion at the lowest frequencies (longest times). In the time domain, this non-analyticity is reflected in the long-time power law tails of Eqs. (8) and (18).

We contrast this with a regular, analytic behavior of $D\omega$ for an ordered ordered or confined geometry. It stems from representing the diffusion propagator as a sum over discrete eigenmodes in a pore (Grebenkov, 2007), cf. Appendices C andD, or as a sumover Blochwaves in a periodic (Dunn and Bergman, 1995; Sen et al., 1994; Sukstanskii et al., 2004; Novikov et al., 2014). In the periodic case, the Bloch eigenstates are labeled by the wave vector k within the first Brillouin zone. The $D\infty$ term corresponds to the lowest band k $= q$, whereas the higher bands with k $= k_n + q$ corresponding to the reciprocal lattice vectors k_n, yield the exponentially decaying contributions $\sim e^{-t/tn}$, with the lowest reciprocal vector k_0 determining the slowest decaying mode $e^{-t=t0}$, see the Eq. (S25) of Ref. Novikov et al. (2014) for a 1d example. For sufficiently long t, keeping only the lowest mode, separated by a finite gap from the rest, is sufficient, which explains an exponentially fast approach of $D\infty$ in Eq. (9), cf. Appendix C. In the frequency domain, calculating the Fourier transform in Eq. (14) of Eq. (9) yields a Lorentzian corresponding to the lowest eigenmode,

$$p=\infty: \mathscr{D}\left(\omega\right) - D_\infty \propto \frac{-i\omega t_0}{1 - i\omega t_0} = -i\omega t_0 + \omega^2 t_0^2 + \ldots, \quad (20)$$

cf. Eq. (D.1). Note the crucial difference from Eq. (19): Eq. (20) is analytic in ω at $\omega = 0$, i.e. it has a regular Taylor expansion with a finite conver gence radius $1/t_0$ in the complex plane of ω.

Since $\langle v(t)v(0)\rangle$ is real-valued, the real part of its Fourier transform (Eq. (15)) must be even in ω. If $D(\omega)$ is also analytic around $\omega = 0$, its Taylor expansion involve only even powers of ω, starting from a quadratic one,

$$p=\infty: Re\,\mathscr{D}\left(\omega\right) \simeq D_\infty + const \cdot \omega^2, \quad |\omega|t_0 \ll 1, \quad (22)$$

in agreement with Eq. (20) and with Appendix D.

In contrast, for the random geometry, the convergence radius of $D(\omega)$ at $\omega = 0$ is zero, due to the non-analytic term $\sim (-i\omega)^\vartheta$ originat ing from the long tail (Eq. (5)). If $\vartheta < 2$, the lowest order behavior (Eq. (21)) will mask the existence of the term $\sim (-i\omega)^\vartheta$, much like the $1/t$ term masks the long-time tail in PG $D(t)$, Eq. (13). In our case of $\vartheta = 1$, $(-i\omega)^\vartheta|_{\vartheta \to 1} \to (-i\omega)ln(-i\omega)$, so already the lowest order in ω in Eqs. (2) and (19) is explicitly non-analytic at $\omega = 0$.

The absolute value (modulus) $|\omega|$ in the real part (Eq. (2)) is essential: Re $D(\omega)$ cannot have odd powers of ω (without the modulus) in its low-frequency expansion (see Fig. 5a) as it must stay even in ω. The only way to have a term linear in frequency in Re $D(\omega)$ is via a non-analytic kink $\sim|\omega|$ (no Taylor expansion at $\omega = 0$), Fig. 5(b).

We emphasize that the absence of linear-in-frequency term in the OG-measured diffusivity (Eq. (21)) for any regular or confined geome-try is a universal consequence of the analytic behavior of $D(\omega)$ in these cases. For naive dimensional estimate would $\sim \omega a^2$ for the OG diffusivity in an impermeable pore of size $\sim a$, similar to the PG estimate $\sim a^2/t$; however, this term enters $D\omega$ with an imaginary i and therefore is not captured by the OG, which is only sensitive to the second-order real term $\sim D_0 \cdot (\omega t_0)^2 \sim \omega^2 a^4/D_0$, where D_0 is the free diffusion coefficient and $t_0 \sim a^2/D_0$, cf. Fig. D.1 and Eq. (D.4) of Appendix D, as well as the Fig. 3 of Ref. Stepisnik et al. (2007). This makes it more difficult to measure the sizes of small confining compartments using OG at low frequencies.

Effect of finite PG pulse duration δ >>t_c

$D(\omega)$is the fundamental characteristic using which one can calculate the effect of any sequence for the lowest (second) order cumulant of the dMRI signal (Novikov and Kiselev, 2011)

$$-lnS = \int \frac{d\omega}{2\pi} q_{-\omega} \mathscr{D}\left(\omega\right) q_\omega + \mathscr{O}\left(g^4\right) \quad (22)$$

where q_ω is the Fourier transform of the integral $q(t) = \int_0^t dt' g(t')$ of the applied Larmor frequency gradient $g(t)$. The finite-pulse PG corresponds to (Callaghan, 1991)

$$q_\omega = \frac{g}{(i\omega)^2}\left(e^{i\omega\delta} - 1\right)\left(e^{i\omega\Delta} - 1\right), \quad (23)$$

where g is the maximum gradient value, and   is the diffusion time, defined as the interval between the front edges of the pulses (whenever it does not cause confusion, we denote this diffusion time $\equiv t$ similar to the narrow-pulse case). The PG measurement becomes a low-pass filter $|q_\omega|^2$ which resolves the time-dependent tail (Eq. (18)) only for $t =$ $\sim 1/\omega \gg \delta$, in which case $q_\omega \simeq (g\delta)(e^{i\omega} - 1)/(i\omega)$ coincides with that for the narrow-pulse limit. While the details of the calculation for the low-pass filter effect will be reported elsewhere (Lee et al., 2015), here we will announce the result for $\vartheta = 1$. The frequency integral in the first term of Eq. (22) is found using Eq. (23) by deforming the inte gration contour in the complex plane of ω from the real axis to the one passing along both edges of the branch cut of $ln\omega$, connecting $\omega = 0$ and $\omega = \infty$ via the lower-half-plane, yielding

$$-lnS = bD_\infty + (g\delta)^2 \cdot AF(\Delta/\delta) + \mathcal{O}\left(g^4\right), \quad (24)$$

$$F(x) = \frac{x^2}{2}ln\left(1 - \frac{1}{x^2}\right) + \frac{1}{2}ln\left(x^2 - 1\right) + x\,ln\frac{x+1}{x-1} \quad (25)$$

where the diffusion weighting parameter $b = (g\delta)^2(- \delta/3)$. Note that $F(1) = 2ln2 \approx 1.38$ and $F(x)|_{x\gg 1} \simeq lnx + \frac{3}{2}$; the latter asymptotic behav ior practically works already for $x \sim 1$. Eqs. (24) and (25) establish the behavior (Eq. (1)) for $\delta \gg t_c$.

Physically, finite PG pulse width δ allows the tail (Eq. (8)) to be manifest only at the time scales $t \gg \tilde{t}_c \sim max\{t_c, \delta\}$. Therefore, finite δ may mask the correlation time t_c, and hence, the correlation length l_c. However, since $F(x)|_x   1 < 1$ and grows monotonically for $x   1$, the time-dependent part $\sim AF(t/\delta)/(t - \delta/3)$ of $D(t)$ defined via $-ln\,S(t) = b   D(t) + \mathcal{O}\left(b^2\right)$, $t \equiv$, decreases slower than $1/t$, asymptotically approaching the $\left[ln\left(t/\tilde{t}_c\right)\right]/t$ behavior (Eq. (1)). Hence, finite δ does not change the overall $(lnt)/t$ dependence (Eq. (1)), only affecting the higher-order corrections $\sim 1/t$ to the "ideal" narrow-pulse $D(t)$.

Table 1 summarizes the results of the Theory section.

Methods

To demonstrate the effect of disorder on the two-dimensional diffusion in the long time limit, we employ an artificial model system mimicking extra-axonal space. By utilizing fibers with a mean diameter larger than axonal diameters by about tenfold, the required diffusion times are increased by about a factor of a hundred, from a few millisec onds to hundreds of ms, which are much easier to observe on a standard clinical MR system. To access such long diffusion times (of up to a second in our case), we use a stimulated echo

sequence to reduce the echo attenuation due to T_2 decay, as we describe in more detail below.

Phantom construction

The diffusion phantom for this study was constructed using Dyneema® fibers held together with a flexible, polyolefin low tempera ture shrinking tube (Fieremans, 2008; Fieremans et al., 2008). The fibers are 17 ± 2.6 μm in diameter and are comprised of an ultra-high-molecular-weight polyethylene (UHMWPE) which is ultrahydrophobic and impermeable to water. Approximately 195,000 fibers were placed in a shrinking tube measuring 8 cm long, and the fiber and tube bundles were placed in a hot water bath with temperature 90 °C for 10 min to shrink the tube. To facilitate the removal of air bubbles, which could contribute to susceptibility artifacts, the tubes were squeezed and shaken as they were shrunk in the hot water bath. The fiber bundle was suspended in the center of a 1.5 L plastic bottle using zip ties. The bottle was then filled with a distilled water solution of 0.09% w/v NaCl to reduce B_1^+ field inhomogeneities.

MRI measurements

Imaging was performed at 16 °C on a 7 T Siemens clinical whole- body MRI scanner using a 28 channel knee coil. A high resolution (1 mm × 1 mm × 1 mm) MPRAGE image was first acquired to locate the presence of any air bubbles within the fiber bundle to determine where best to place the diffusion tensor imaging slices. DTI was carried out using the stimulated echo acquisition mode (STEAM) sequence which allows for long diffusion times while minimizing echo attenua tion caused by T_2 relaxation. Twenty five measurements were performed at b values of 0 and 1 ms/μm^2 in 20 directions, each with a constant TE = 68 ms, δ = 17.5 ms, and a TM ranging from 10 ms to 980 ms, corresponding to diffusion times t = TE/2 + TM of 44 ms to 1014 ms. Two slices of resolution 2.2 mm × 2.2 mm × 10 mm were used. The fiber bundle was placed parallel to the B$_0$ field to eliminate the possibility of susceptibility-induced internal field inhomogeneities produced by the fibers.

Monte Carlo simulations in the intra- and extra-axonal spaces

We generate three types of impermeable two-dimensional disk packings – one to simulate our fiber phantom, one to simulate a periodic packing, and another to simulate white matter. The disk packing mim icking the fiber phantom is comprised of $N \approx 10,000$ disks with a radius of 8.5 ± 1.3 μm packed to a density of 75%. This density is chosen as it best matches the FA value of 0.54 calculated for the phantom for $t > 700$ ms. For the periodic packing we generate a lattice of disks with a radius 8.5 μm packed to a density of 72%; a higher density lattice is unachievable for our current simulation.

For the white matter, we generated three different packings based on the axon inner diameter distributions in sectors 2, 4, and 6 of the rhesus monkey corpus callosum determined by Lamantia and Rakic (1990), and packed to a density of 70% for all sectors, i.e. extra-axonal space occupies fraction $\varphi_{ext} = 0.3$ of the volume. To determine these distributions, we first digitized the histograms provided in Lamantia and Rakic (1990) for the internal axonal diameters 2r. The correspond ing external diameters 2r$_{ext}$ were found by dividing 2r by the myelin g-ratio $g_m = r/r_{ext} = 0.6$ (Rushton, 1951) which we assumed to be the same for all

simulated axons. We do not account for the possible shrinkage of the axons due to a conflicting evidence of the extent of this effect; our results can be readily rescaled to account for the shrink age. These external diameters were then used for randomly packing N impermeable disks for the simulations, see Supplementary figs. S1–S3.

All packings (except for the periodic one) were generated using a collision-driven molecular dynamics simulation script written by Donev et al. (Donev et al., 2005b,c).

To simulate the narrow-pulse cumulative diffusion coefficient $D_{ext}(t)$ in the extra-axonal space, 1×10^6 tracers are placed randomly outside the disks, and allowed to perform 2d Brownian motion restricted by the impermeable disk walls, following the Monte Carlo dynamics previously described in detail (Fieremans et al., 2010). Briefly, during each time step dt, a tracer steps a fixed distance dr given by $\sqrt{2dD_0dt}$ with $d = 2$ in a randomly chosen direction. For the phantom simulation, d$t = 7.5 \times 10^{-4}$ ms, and for the white matter simulation, dt $= 7.5 \times 10^{-5}$ ms, corresponding to step lengths of 0.0775 μm and 0.0245 μm, respectively. If a tracer encounters a barrier, it will elastically reflect off the barrier. We verified our MC algorithm by simulating $D(t)$ inside one impermeable cylinder, and obtained a perfect agreement with the exact result, see Fig. C.1 in Appendix C. Expanding upon this, we also simulate the intra-axonal $D(t)$ within the impermeable cylinders of all 3 sectors assuming inner radii based on the reported values in Lamantia and Rakic (1990), which agrees with the asymptotic behavior (Eq. (27)) below. For all simulations, $D_0 = 2$ μm^2/ms.

The time-dependent diffusion coefficient in direction n is calculated via Eq. (3), with$\delta x(t)$ $\equiv$R × n, where R(t) is the cumulative displacement for a given tracer over the Monte Carlo time t. In this paper, n is taken in the two orthogonal directions separately, and the resulting mean square displacements are further averaged between the two directions to yield the isotropic diffusion coefficient transverse to cylinders (disks).

We do not simulate the diffusion-weighted signal, as the effect of the finite gradient pulses can be derived from the narrow-pulse MC using Eqs. (24) and (25). This makes results more reliable, since simulating the signal with finite pulses involves adding oscillating phases, which notably reduces the precision.

Model for diffusion inside axons and for overall D(t)

For comparing the roles of extra- and intra-axonal spaces, we use a common assumption of effectively impermeable axonal walls (Assaf et al., 2008; Alexander et al., 2010; Zhang et al., 2011) which is reason able given thick myelin layers covering axons within major fiber tracts. Hence, the total time-dependent diffusion coefficient (Eq. (3)), defined via the second cumulant of the total signal (Appendix E), is given by the weighted average of the diffusion coefficients of the intra- and extra- axonal compartments (Fieremans et al., 2010):

$$D\left(t\right) = f_{int}D_{int}\left(t\right) + f_{ext}D_{ext}\left(t\right), \quad (26)$$

where $f_{ext} + f_{int} = 1$ are the fractions of intra- and extra-axonal water, and $D_{ext}(t)$ is simulated as described above. We assume that water within myelin is effectively invisible in diffusion due to its short T_2.

We model diffusion in the intra-axonal space in the narrow-pulse limit using the impermeable cylinder model (Stepišnik, 1993; Callaghan, 1995). As it follows from our analysis of the exact solution in Appendix C, for the relevant diffusion times, within each cylinder with internal radius a the diffusion coefficient is very well approximated by its asymptotic limit $D(t) \simeq a^2/4t$, Eq. (C.4) and Fig. C.1. We obtain $D_{int}(t)$ from impermeable cylinders according to the distribution of axonal sizes from Lamantia and Rakic (1990). As a result, the diffusion coefficient from inside the axons entering Eq. (26) is found as

$$D_{int}(t) \simeq \sum_{i=1}^{N} \frac{\phi_{int}^{(i)}}{\phi_{int}} \frac{r_i^2}{4t}, \quad \phi_{int} = \sum_{i=1}^{N} \phi_{int}^{(i)}, \quad \phi_{int}^{(i)} = \frac{\pi r_i^2}{V}. \quad (27)$$

In terms of the moments $\langle r^n \rangle$ of the axonal size distribution,

$$D_{int}(t) \simeq \frac{\langle r^4 \rangle / \langle r^2 \rangle}{4t}. \quad (28)$$

With a fixed value of the g-ratio, the fractions φ_{ext}, φ_{int}, and $(1/g^2 - 1)\varphi_{int}$ are the volume fractions of extra-axonal water, intra-axonal water and myelin, correspondingly, such that $\varphi_{ext} + \varphi_{int}/g^2 = 1$. The water fractions entering Eq. (26) are

$$f_{ext} = \frac{\phi_{ext}}{\phi_{int} + \phi_{ext}}, \quad f_{int} = \frac{\phi_{int}}{\phi_{int} + \phi_{ext}}. \quad (29)$$

Hence, for sectors 2, 4, 6, $\varphi_{ext} = 0.3$, $\varphi_{int} = 0.7 \cdot 0.6^2 = 0.252$, so that $f_{ext} = 0.54$, $f_{int} = 0.46$ in Fig. 11.

Results

Identifying the logarithmic singularity, Eq. (1)

The eigenvalues from the experimentally measured diffusion tensor in our fiber phantom are plotted in Fig. 6a, with the principle eigenvalue, λ_1, shown by the circles, and the transverse eigenvalues, λ_2 and λ_3, shown by the triangles and squares, respectively. Since the direction of λ_1 is aligned parallel to the fibers for all t, it corresponds to practically unrestricted diffusion, as seen in the figure. However, as λ_2 and λ_3 are measured transverse to the bundle, they indeed decrease with t due to geometric restrictions by impermeable fibers. Note that differences between λ_2 and λ_3 are probably the result of the eigenvalue repulsion due to noise. The larger errorbars associated with these two eigenvalues likely arise due to the Gibbs ringing present in transverse direction.

We see similar behavior in our simulation data as indicated by the solid black line. To better represent the experimental conditions, which were at 16 °C rather than 20 °C, we applied a rescaling factor of $1.8/2.0 = 0.9$ to $D(t)$ and $1/0.9$ to t based on the free $D_0 = 1.8$ μm^2/ms for water at 16 °C (Tofts et al., 2000).

To study the nature of the time dependence, the transverse eigen values are averaged together to obtain the isotropic two-dimensional component of the transverse diffusivity

$$D_\perp(t) = \frac{\lambda_2 + \lambda_3}{2}. \quad (30)$$

Taking the average (30) significantly reduces bias due to noise. Indeed, the effect of eigenvalue repulsion is exactly compensated by taking the mean of eigenvalues in a 2×2 tensor; the residual repulsion in our 3×3 case coming from the presence of λ_1 is small, since $\lambda_2 - \lambda_3 \ll \lambda_1 - \lambda_{2,3}$. We use the narrow-pulse PG notation (Eq. (3)) in Eq. (30) since we are studying t ~ 100 − 1000 ms, orders of magnitude longer than $\delta = 17.5$ ms.

The approach of $D_\perp(t)$ towards D_∞ is shown in Fig. 6b, where D_∞ is determined via a fit to Eq. (1). The fit parameters D_∞, A, and $\tilde{t}_c$ are shown in the "Experiment" column of Table 2. We also observe that the value $\tilde{t}_c$ is close to δ, so while the agreement with t_c from MC simulations is very good, this fit parameter value might be rather indicating the "filter effect" of a finite-δ PG; besides, it is generally hard to obtain reliable fit results for quantities under the logarithm.

Even on a qualitative level, it is clear that the slope of the experimen tal curve is not constant. Hence, the time-dependence clearly deviates from $1/t$, as the fit to $D_\infty + c/t$ shows. This fit also looks particularly poor due to the double-logarithmic axes exaggerating the small devia tions the fit has to the data. The fit to Eq. (1) shown by the black dashed line is considerably better (the R^2 value increases from 0.82 to 0.95). This is the first indication of the anticipated logarithmic singularity (Eq. (1)). The simulation data (blue dotted line) shows a trend similar to the experimental data, with the parameters summarized in the "MC: Phantom" column of Table 2.

Another way to see the effect of the $(lnt)/t$ dependence is presented in Fig. 7. Here, the transverse component (Eq. (30)) is plotted with respect to $1/t$ (Figs. 7a, c) and with respect to $ln(t/t_c)/t$ (Figs. 7b, d). The top row shows Monte Carlo simulated fiber phantom diffusion data, and the bottom row is the experimental data. As is evident from Fig. 7a, the slope of the data keeps changing with respect to $1/t$, indicat ing that the behavior is slower than 1/t. However, when the data is plotted with respect to $ln(t/t_c)/t$, as in Fig. 7b, this curve straightens out, indicating the logarithmic singularity. We also see this trend in our experimental data as shown in Figs. 7c and d.

In contrast, Fig. 8a shows the $D(t)$ from the exterior of the simulated square lattice of disks, exhibiting a 1/t dependence as expected from Eq. (13).

Identifying the dynamical exponent ϑ

Alternatively, we can determine the instantaneous diffusion coeffi cient $D_{\text{inst}}(t)$ using Eq. (4) from both experimental and simulated data, and confirm the value $\vartheta = 1$ of the dynamical exponent, which is equivalent to the singular behavior (Eq. (1)). To do this, we use a Savitzky–Golay (Savitzky and Golay, 1964) second order polynomial smoothing procedure

written in house using Matlab (Mathworks, Natick, MA) to smooth and differentiate our data.

The results of this procedure are shown in Figs. 8 and 9.

In Figs. 8a and b, $D(t)$ and the derived $D_{\text{inst}}(t)$ is shown for the Monte Carlo simulated data for the square lattice disk pack. The semilog scale in Fig. 8b indicates that, in contrast to the disordered samples, $D_{\text{inst}}(t)$ approaches its D_∞ value in the $\sim exp(-t/t_0)$ fashion, as expected from Eq. (9), corresponding to the dynamical exponent $\vartheta = \infty$. A fit of this data (shown by the black line) reveals a $t_0 \approx 3.1$ ms, which is somewhat small compared to the diffusion time of ≈ 20 ms across the lattice constant. This smallness is similar to what is observed in the $d = 1$ lattice (Novikov et al., 2014).

Fig. 8c contrasts $D_{\text{inst}}(t)$ for both the periodic and random geometries, plotted with respect to 1/t. Note that $D_{\text{inst}}(t)$ for both geometries have markedly different approaches to their corresponding D_∞ values, indicating the strong sensitivity of $D_{\text{inst}}(t)$ to order/disorder at long times.

In Fig. 9, to emphasize the t^{-1} behavior, we plot $D_{\text{inst}}(t)$ as function of 1/t for our experimental and simulated data, respectively. In Panel (a), different symbol shapes indicate different Savitzky–Golay smoothing window sizes (see legend). We note that at long times (i.e. small 1/t), no matter how much the data is smoothed, there is an asymptotically linear dependence on 1/t (indicated by the solid black line), showing that $D_{\text{inst}}(t)$ approaches its D_∞ limit as $\sim 1/t$, in agreement with the exponent $\vartheta = 1$ in Eq. (5), expected in a 2d random packing geometry.

In Fig. 9b, the same $D_{\text{inst}}(t)$ as in Fig. 8c is plotted for the long t (small t^{-1}). For MC data, we use adaptive Savitzky–Golay window growing with t from 21 to 2001 MC time points.

While it may seem that the time dependence of the blue curve in Fig. 8c is far from t^{-1}, this is only because the shortest times are overemphasized due to the t^{-1} inversion of the time axis. The asymptotically linear dependence on t^{-1} becomes evident in Fig. 9b, which displays about 90% of all our MC time points, corresponding to 100 ms t 1000 ms.

What does this mean for diffusion transverse to WM fibers? Since diffusion time scales as length squared, and given that axonal diameters are about 10 times smaller than those of the Dyneema fibers, Fig. 9 suggests that the long-time 1/t tail in $D_{\text{inst}}(t)$ and, thereby, the logarithmically enhanced behavior (Eq. (1)) would manifest themselves in WM as long as the diffusion time is about 100 times smaller than its onset of ≈ 100 ms in Fig. 9, i.e. for t 1 ms in vivo, cf. Table 2. This, for all practical purposes, covers all MRI-observable diffusion times. From Fig. 9, we also note that the dynamical exponent $\vartheta = 1$ becomes manifest when $D_{\text{inst}}(t)$ is within roughly 10% of D_∞ for both experiment (a) and simulation (b). Our MC simulations for the realistic axonal geometries discussed below and shown in Fig. 11 are in agreement with the above estimates.

Dominant role of extracellular water in OG diffusion transverse to neuronal fibers

Let us now turn to the recent OG experiment (Portnoy et al., 2013), whose data we replot in Fig. 10. In this figure, the frequency dependent diffusion coefficient was measured inside an ex vivo rat hippocampus with 10 cosine modulated diffusion gradients ranging from 67 Hz to 1 kHz on a 600 MHz Bruker spectrometer. The data shown is from the stratum radiatum section of the hippocampus transverse to the fibers. We can clearly see the linear dependence (Eq. (2)) at low ω (as long as Re$D(\omega)$ is within about 20% of D_∞), corresponding to the dynamical exponent $\vartheta = 1$. From that, it follows that the structural exponent $p = 0$, corresponding to short range disorder, in agreement with our correlation analysis performed in a different brain region within a single fiber tract (splenium, cf. Figs. 3f and 4). As the ~ |ω| behavior occurs for up to 0.4 kHz, the corresponding t_c 1 ms and the disorder correlation length l_c 1 μm. This suggests that short range disorder in fiber packing with $l_c \sim 1$ μm is likely to be a universal feature of brain anatomy com mon to all fibrous regions, making our results on diffusion in random 2d packings widely applicable.

Furthermore, we observe no trace of the "parabolic" dependence of Eqs. (21) and (D.4) from water presumably confined within fibers or elsewhere. This is not surprising, as the linear term wins over the quadratic one at low enough frequency (cf. Fig. 5b):

$$c_1|\omega|+c_2\omega^2 \simeq c_1|\omega|, \quad \omega \to 0. \quad (31)$$

Therefore, at low ω, due to the structural disorder, the dispersive contribution to $D(\omega)$ of the hindered component wins over that of the fully restricted component in a 2d geometry. In otherwords, the contribution of the confined water to the overall $D(\omega)$, and with that, any information about the inner fiber diameters, is practically unobservable with diffusion measured using OG transverse to the fibers in the small ω limit.

We note that extra-axonal ω also has regular contributions, such as ω^2 further increases ω to "catch" the ω^2 term on the background of |ω|, it does not help to quantify internal axonal diameters without knowing which part of this term comes from intra-axonal water.

In Appendix F we argue that the |ω| behavior in $D(\omega)$ is determined by the random packing geometry irrespective of the exchange rate τ_{ex}^{-1} between intra- and extra-axonal compartments, and that OG is thus asymptotically insensitive to internal axonal diameters at low ω even when exchange is present.

Dominant role of extra-axonal water in narrow-pulse PG diffusion transverse to axons

Consider first the common assumption of negligible exchange, which is likely to hold for major fiber tracts. In this limit, the overall diffusion coefficient is given by Eq. (26). We now show, similar to the frequency case (Eq. (31)), that the extra-axonal contribution is domi nant at long times. Here we focus on the narrow-pulse PG limit in order to understand the ideal situation. In Discussion section, we will use these results to argue that for finite δ, the extra-axonal contribution becomes relatively even more important and biases axonal diameter results, Fig. 2.

The extra-axonal (lnt)/t contribution (Eq. (1)) to the overall narrow- pulse diffusion coefficient (Eq. (26)) should become gradually more pronounced, due to its slower decrease with time, than the $1/t$ contribution of the confined intra-axonal water, Eq. (28), since

$$\tilde{c}_1 \frac{1}{t} + \tilde{c}_2 \frac{int}{t} \simeq \tilde{c}_2 \frac{int}{t}, \quad t \gg t_c. \quad (32)$$

The extra-axonal dominance should be less dramatic for PG than for OG, Eq. (31), as lnt is a relatively slowly growing function.

How significant is this effect for realistic axonal packings? To address this question quantitatively, we calculate the time dependence of the diffusion coefficient (Eq. (26))

$$D(t) - D_\infty = f_{int} D_{int}(t) + f_{ext}\left(D_{ext}(t) - D_\infty^{ext} \right), \quad (33)$$

where the overall $D_\infty = f_{ext} D_\infty^{ext}$. In Fig. 11, we show the results of Monte Carlo simulations for $D_{ext}(t)$ for the three cylindrical (disk) packings based on sectors 2, 4, and 6 of the rhesus monkey corpus callosum, as well as analytical and numerical results for $D_{int}(t)$ (see Methods section). The left column of Fig. 11 shows small fragments of the cylinder packs used in the simulation with the corresponding histograms of the radii (Lamantia and Rakic, 1990) in the center column (for full packings, see Supplementary figs. S1–S3). The main results are shown in the right column, where we plot the first and the second terms of Eq. (33) along with the total $D(t) - D_\infty$.

In all three cases, the extra-axonal contribution dominates the over all time dependence at practically relevant times ($t \quad 1$ ms). The long time limit begins at approximately 1 ms, meaning that this dominance is always present, as already anticipated from the results of Fig. 9. At the experimentally feasible time scales of $t = 10$ and 100 ms, the t-dependent part of $D_{ext}(t)$ comprises over 80% of the total $D(t)$ for all sectors as seen in Table 3, and logarithmically grows with t.

In other words, similar to the OG case, the intra-axonal compartment becomes asymptotically invisible on the background of the extra-axonal contribution.

The results of fitting of $D_{ext}(t)$ to Eq. (1) are presented in the last three columns of Table 2. As the three-parameter fitting can become un stable, especially for t_c entering under the weakly-varying logarithm, we first derive the corresponding instantaneous diffusion coefficient (Eq. (8)) using the Savitzky–Golay procedure outlined above, which allows us to eliminate t_c (Supplementary fig. S5); after D_∞ and A are fit, they are fixed in the fitting of $D_{ext}(t)$ to Eq. (1) in order to obtain t_c. We observe that the correlation length $l_c \approx \langle r_{ext} \rangle$ does not parametrical ly exceed the mean external axonal radius. This indicates that local order due to a mutual "repulsion" of disks in all our packings disappears already at the level of nearest neighbors. (Presumably, packing at a higher density may lead to emergence of short range order, $l_c \gg \langle r_{ext} \rangle$.) We also note an approximate scaling $A \sim l_c^2$, Supplementary fig. S4, expected from the dimensional considerations: At $t \gg t_c$, the t-independent length scale that the system still "remembers" after the coarse-graining is the correlation length

$l_c = \sqrt{2 d D_\infty t_c}$, and A has dimensions of (length)^2. This scaling is only approximate since the plateau $\Gamma(k)|_{k \to +0}$ is governed not only by l_c^2 but by the packing details, see Fig. 4 and an estimate at the end of Appendix A.

If exchange is present, our argument in 6 translated to the time do main suggests that the (lnt)/t term due to extra-axonal space geometry will similarly prevail for the slow exchange $\tau_{ex} > t_c$, and will apply to all water molecules in the fast exchange limit $\tau_{ex} < t_c$.

Discussion: what do we measure with dMRI transverse to axonal fibers?

Quantifying μm-level structure of neuronal tracts in vivo has been brought to the forefront of neuroscience research primarily due to the axonal diameter mapping (ADM) concept, developed within AxCaliber framework (Assaf et al., 2008; Barazany et al., 2009) and their exten sions (Alexander et al., 2010; Zhang et al., 2011). Their common theme is the focus on the intra-axonal compartment (assuming no exchange), which is typically done by approximating axons as imper meable cylinders, and building on exact solutions (Neuman, 1974; Stepišnik, 1993; Callaghan, 1995). Water diffusion in the extra-axonal space in all of the above approaches is assumed to be Gaussian (time- independent).

Our findings of the unexpectedly dominant role of the time-dependence of dMRI signal from extra-axonal water prompt us to reconsider the applicability and interpretation of ADM.

ADM in the narrow-pulse limit δ < t$_c$

In Appendix E, by attributing the time-dependencies of both $D_{int}(t)$ and $D_{ext}(t)$ in Eq. (33) to the intra-axonal water, i.e. assuming Gaussian extra-axonal diffusion, up to order $\mathscr{O}\left(q^2\right)$ in the cumulant expansion we obtain an apparent internal axonal radius $r_{app}(t)$ growing with diffusion time t:

$$r_{app}^2(t)\big|_{\delta \ll t_c} \simeq \frac{\langle r^4 \rangle}{\langle r^2 \rangle} + 4A \cdot \frac{f_{ext}}{f_{int}} \cdot ln\frac{t}{t_c}. \quad (34)$$

While the first term in Eq. (34) reflects the volume-weighted contri bution of water inside all axons, cf. Eq. (28), the second term comes from the singular time-dependent contribution (1) of the extra-axonal water. It results in the overestimation of the value of the axonal radius. This bias has been illustrated in Fig. 2 of Introduction, where $r_{app}(t)$ (dashed lines) is calculated from Eq. (34), using A and t_c determined from Fig. 11, Table 2. Based on these parameters, the second term in Eq. (34) exceeds not only $\langle r \rangle^2$ but even $\langle r^4 \rangle / \langle r^2 \rangle$, so that the apparent internal axonal radii could be significantly biased by the extra-axonal contribution. Indeed, as seen from the second row of Table 3, the calculated value of r_{app} is roughly 3–4 times greater than $\langle r \rangle$ for all three corpus callosum sectors.

Furthermore, our analysis in Appendix E shows that including the $\mathscr{O}\left(q^4\right)$ terms leads to the further increase of the apparent $r_{app}(t)$, making it grow even faster with time, as $(tlnt)^{1/4}$, Eq. (E.9), which occurs due to the corresponding (lnt)/t behavior of the kurtosis $K_{ext}(t)$ in the

extra-axonal space, Eq. (E.4). While being numerically too small to affect fits of quantities such as axonal (or neurite) water fraction especially at the clinical times $t \sim 10 - 100$ ms (Assaf et al., 2008; Jespersen et al., 2007, 2010; Fieremans et al., 2010), $K_{ext}(t)$ generally cannot be neglected for more subtle techniques such as axonal diameter mapping, since all the (time-dependent) corrections originating from finite axonal diameters are comparably small, cf. Fig. 11.

To get a sense when Eq. (34) applies, let us employ dimensionless time and Larmor frequency gradient variables

$$\bar{t} = \frac{t}{t_c} = \frac{\Delta}{t_c}, \quad \bar{\delta} = \frac{\delta}{t_c}, \quad \bar{g} = \frac{g}{g_r}; \quad g_r = \frac{D_0}{r^3} \sim \frac{1}{r t_c} \quad (35)$$

where the disorder correlation time scale $t_c \sim r^2/D\infty \sim \tau \, r^2/D_0 \sim 0.1 - 1$ ms is practically similar to the diffusion time τ_D within axon with typical radius r (Table 2), and g_r is the characteristic scale for the Larmor frequency gradient needed to efficiently probe distances $\sim r$. Using the variables (Eq. (35)), we make order-of-magnitude estimates by dropping all dropping all coefficients $\mathcal{O}(1)$ in Appendis E:

$$-ln S_{int} \sim \alpha^2 + \mathcal{O}(\alpha^4), \quad -ln S_{ext} \sim \alpha^2 \left(\bar{t} + \bar{A} \, ln \, \bar{t} \right) + \mathcal{O}(\alpha^4), \quad (36)$$

where $= A/r^2 \sim 0.1$–1, and the dephasing strength $\alpha = qr = gr\delta \equiv \bar{g}\bar{\delta}$ is usually small, as diffusion gradients are generally weak relative to the scale gr. Indeed, the scale $gr \approx 20(\mu m \cdot ms)^{-1}$ for $2r = 1 \mu m$, assuming free axoplasm diffusivity $D_0 = 2.4 \mu m^2/ms$ (Beaulieu, 2002), where-as $g = \gamma \cdot 40mT/m = 0.0107(\mu m \cdot ms)^{-1}$ for a typical clinical scanner, and $g \sim 0.1(\mu m \cdot ms)^{-1}$ for animal systems. This makes $\bar{g} \sim 10^{-2} - 10^{-3}$; assuming $\delta < t_c$ makes $\alpha \ll 1$.

We can see that in the $\bar{\delta} < 1$ limit considered in Eq. (36), the three dimensionless quantities t, δ, and g enter only in the two combinations: α and $\bar{t}$. Hence, the phase diagram in this limit is two-dimensional, and is schematically outlined in the left panel of Fig. 12. The extra-axonal signal is effectively suppressed when $\alpha^2 \bar{t} \gg 1$, i.e. above the green line $\alpha \sim \bar{t}^{-1/2}$. As $\alpha \ll 1$, the intra-axonal signal is practically never small (we are always below the red line). The ADM applies in the green shaded region where the extra-axonal contribution can be neglected, while the intra-axonal signal is still not too small. However, below the green line (regime I), when both S_{int} and S_{ext} are not exponentially suppressed, the above results of Appendix E apply, and Eq. (34) becomes asymptotically exact for $\alpha \ll \bar{t}^{-1/2}$. While it is advan tageous for the ADM to increase the diffusion time $\bar{t}$, the right edge of the phase diagram is limited by T_2, so that t 100 ms, $\bar{t} \lesssim 10^2 - 10^3$, and so for $\bar{\delta} < 1$, we are practically always in the regime I, $\alpha \ll \bar{t}^{-1/2}$, where Eq. (34) asymptotically applies.

ADM on clinical scanners, $\delta \gg t_c$

Clinical acquisition employs wide pulses, with duration δ 10 ms exceeding both the diffusion time $\tau_D = r^2/D_0$ across the inner radius of a typical axon, and the correlation time t_c in the extra-axonal space. In this limit, the above analysis gets modified. It turns out that diffusion attenuation (at a given *b*-value) becomes generally weaker in both intra- and extra-axonal space. However, while extra-axonal contribu tion changes only logarithmically, $\ln(t/t_c) \rightarrow ln(\ /\delta)$, cf. Eq. (24), the intra-axonal attenuation becomes smaller by the factor $\tau_D/\delta \ll 1$. Physically, this ineffectiveness of diffusion gradients stems from the motional narrowing of the transverse relaxation rate $R_2^* \sim (gr)^2 \cdot \tau_D$ within an axon under the applied gradient.

To get an idea of just how insensitive clinical systems are to typical axonal sizes, we find the attenuation (Neuman, 1974)

$$ln S_{int}\big|_{\delta \gg \tau_D} \simeq \frac{7}{96}\frac{g^2 r^2}{D_0} \cdot 2\delta \approx 2.17 \cdot 10^{-5} \quad (37)$$

where we used $g = 0.0107(\mu m \cdot ms)^{-1}$ corresponding to 40 mT/m gradient, $D_0 = 2.4$ μm^2/ms, $\delta = 50$ ms, and a typical internal axonal diameter $2r = 1$ μm. Even with the r^4 scaling, the very large axons with $2r = 4$ μm give $- lnS_{int} \approx 0.0056$, i.e. less than 1% attenuation.

For dimensionless estimates, the variables (35) are $\bar{g} \sim 10^{-3}$; $\bar{t} \equiv\ /t_c\ 10^2\text{--}10^3$; $\bar{\delta} \sim 10\text{--}10^2$. The contributions to signal $S = f_{int}S_{int} + f_{ext}S_{ext}$ are Eqs. (37) and (24)–(25) respectively,

$$-ln\, S_{int} \sim \bar{g}^2\, \bar{\delta}, \quad -ln\, S_{ext} \sim \bar{g}^2 \bar{\delta}^2\, \bar{t} + \bar{g}^2 \bar{\delta}^2\, \bar{A}\, F\left(\bar{t}\, /\, \bar{\delta}\right). \quad (38)$$

The full phase diagram is now 3-dimensional. To simplify it and to gain further intuition, we assume $\bar{t} \sim \bar{\delta}$, i.e. pulses are as wide as possi ble, $\delta \sim\ $, which is often the case. This leaves $\bar{t}$ and $\bar{g}$ as variables, cf. right panel of Fig. 12. The extra-axonal signal is suppressed and ADM applies above the green line, scaling as $\bar{g} \sim \bar{t}^{-3/2}$. Below this line (regime II), both S_{int} and S_{ext} are not suppressed, and we can again use their cumulant expansions to estimate the role of *t*-dependence of S_{ext} in the ADM.

Restoring numerical coefficients in Eq. (38), expanding up to $\mathcal{O}\left(\bar{g}^2\right)$ similar to Appendix E, and assigning all *t*-dependence to $- \ln S_{int} \propto r_{app}^4 (\Delta, \delta)$, cf. Eq. (37), as it would effectively occur in a fit to ADM models, we obtain in regime II

$$r_{app}^4 (\Delta, \delta)\,\big|_{\delta \gg t_c} \simeq \frac{\langle r^6 \rangle}{\langle r^2 \rangle} + \frac{48}{7}\frac{f_{ext}}{f_{int}} \cdot D_0 \delta \cdot AF (\Delta/\delta). \quad (39)$$

The apparent axonal radius according to Eq. (39) is shown in Fig. 2 (solid lines). It exceeds the one from Eq. (34) due to the relative small ness of the intra-axonal contribution (Eq.

(37)) in the $\delta \gg t_c$ limit. For the corpus callosum parameters determined from MC, Table 2, the intra-axonal term $\langle r^6 \rangle / \langle r^2 \rangle$ of Eq. (39) gives a less than 1% contribution to the right-hand side. Therefore, the apparent radii r_{app} found in regime II of Fig. 12, third line of Table 3, exceeding the ones from histology (Lamantia and Rakic, 1990) by almost an order of magnitude, are completely determined by the extra-axonal geometry, embodied in the parameter A, Eq. (A.4), and have little to do with intra-axonal diameters. This observation makes studying the effect of spatial correlations of axonal packing on the dMRI signal highly relevant. It is also likely to explain the noted overestimation of axonal diameters (Alexander et al., 2010; Zhang et al., 2011), in ADM at clinical gradient strengths, when the overall signal is mainly determined by its few lowest-order cumulants (regime II). The cumulant expansion performs within its convergence radius, $b < b_c$ (Kiselev, 2010), which can be roughly estimated as $b_c \approx 3$ ms/μm^2 for the white matter.

In this picture, the main contribution to Eq. (39) coming from the term $\sim A$ growing with the external radii (Table 2), can rationalize correlation between r_{app} and neuronal signal propagation speed (amount of myelin) (Horowitz et al., 2014). The observed decrease of r_{app} with increasing gradients (Huang et al., 2015) is consistent with moving up-wards from regime II towards the green domain in Fig. 12. Dedicated suppression of extra-axonal contribution (Dhital et al., 2014) requires strong gradients, or the stimulated echo weighting. OG measurements, much like PG, strongly benefit from larger axons, such as in spinal cord (Xu et al., 2014). For OG, it is essential to reach high enough ω such that $D(\omega)$ saturates, and ideally to combine this with axonal water fraction estimation (at high b) in the $t \to \infty$ limit, in order to be able to resolve intra- and extra-axonal contributions in the view of the remark after Eq. (31).

Mesoscopic effects: a novel kind of dMRI contrast

The unexpectedly strong contribution of the extra-axonal water to the overall time-dependent diffusion cumulants such as diffusion coefficient and kurtosis, and their sensitivity to the fiber packing embodied in the structure correlation function $\Gamma(k)$, opens up a possibility to sense pathologies affecting the extra-axonal space geometry, such as demyelination and axonal loss, as well as possibly signal propagation speed, with diffusion.

Overall, our work brings to the forefront the mesoscopic effects — i.e. effects of spatial arrangement, correlations and structural disorder — in dMRI. Embracing the complexity of cellular architecture at the mesoscopic scale, intermediate between the molecular level (where local NMR parameters originate) and the macroscopic MRI resolution, offers a variety of physical effects relevant to quantifying tissue architecture. Mesoscopic transport, an area of condensed matter physics investigating the role of disorder in transport properties of complex systems, has enjoyed over a half-century of development motivated primarily by the electron conductivity (Anderson, 1958; Abrahams et al., 1979; Bouchaud and Georges, 1990; Kamenev, 2011; Mott and Davies, 1971; Shklovskii and Efros, 1984). This spurred the development of sophisticated methods and physical intuition which extends far beyond semi-conductor physics. The rapidly improving quality of dMRI acquisition is now enabling us to investigate the mesoscopic effects in vivo (Novikov et al., 2014). This novel kind of sensitivity to structure requires going beyond the conventional modeling paradigm of

Gaussian com partments (with or without exchange), such as the Kärger model (Fieremans et al., 2010) and its multiexponential anisotropic extentions (Panagiotaki et al., 2012). The focus of the mesoscopic approach is on the averaging of the diffusion propagator over the disorder in positions of restrictions at the mesoscopic scale. Remarkably, methods developed previously in a different physical context are now becoming relevant to neuroscience and to noninvasive imaging, with an exciting prospect of identifying highly specific markers of pathology in neuronal tissue.

The mesoscopic effects may also affect the intra-axonal contribution to the overall $D(t)$ and to r_{app}, cf. Eqs. (34) and (39). The tail of the axonal diameter distribution strongly affects the moments $\langle r^4 \rangle$ and $\langle r^6 \rangle$, giving a large weight to a relatively small number of axons with largest diameters. Hence, these contributions are susceptible to the mesoscopic fluctuations governed by the tail of the distribution. This general phe nomenon of rare disorder configurations determining the measurement outcome has parallels with similar effects found in hopping conduction in disordered semiconductors, kinetics of reaction-diffusion systems, and other phenomena in disordered media (Lifshitz, 1964; Mott and Davies, 1971; Shklovskii and Efros, 1984). In our case, an accidentally large number of thicker axons, or even a few very thick axons, may sig nificantly skew the overall $D_{int}(t)$ for a particular voxel. This could lead to strongly enhanced variations (relative to those expected based on the measurement noise alone) in the corresponding parametric maps. Addressing how the mesoscopic fluctuations affect the measurement, how representative is a "typical" voxel in a region of interest, how reliably we know the axonal diameter distribution (Lamantia and Rakic, 1990) and its tail (the hardest to determine), and how wide the histograms of the inferred parameters are due to the sensitivity to the tail of the distribution, deserves a separate investigation.

Generalizations

So far, we considered the parallel fibers geometry. What about non- parallel fibers, such as in fiber crossing regions or in gray matter? As long as the neurites are randomly positioned, we expect that the dy namical exponent $\vartheta = 1$ in the extra-neurite space will persist, and hence the behavior of Eqs. (1) and (2) will still be valid. This can be understood from the analysis based on Eq. (6) in $d = 3$ dimensions, where the structural exponent $p = -1$ has been anticipated in the random-rod geometry, cf. Fig. 2 of Novikov et al. (2014). Qualitatively, the spatial fluctuations of the local diffusion coefficient brought by the randomly-positioned straight restrictions ("rods") in 3d behave in the same way as those due to randomly positioned "compact" restrictions in 2d. Thus, the change in the structural exponent, $0 \rightarrow -1$, exactly compensates the change in the dimensionality, $2 \rightarrow 3$, in the calculation of ϑ. Proving that the neurites can indeed be thought of as randomly positioned straight segments with $p = -1$ in three dimensions will re quire a detailed correlation analysis of a 3d histology reconstruction, similar to what we have done in a 2d case, Fig. 4.

The overall time- or frequency-dependence in the case of non-parallel fibers may be generally dominated by the intra-neurite water due to the $d = 1$-dimensional short range disorder ($p = 0$) along the neurites, leading to $\vartheta = 1/2$. This means that, practically, when diffusion is measured in the direction with a notable diffusion contribution along the

neurites, the slower, $\sim t^{-1/2}$ decrease from $D_{int}(t)$ will dominate the $(lnt)/t$ decrease from $D_{ext}(t)$, similarly to $|\omega|^{1/2}$ dominating $|\omega|$ in the OG case (Novikov et al., 2014). Hence, the behavior in Eqs. (1) and (2) considered here is most relevant in the case when diffusion is measured at the right angle to a major fiber tract (with well aligned fibers), which is indeed the case in most applications of axonal diameter mapping techniques.

We also note that a similar time-dependent contribution from the extra-neurite water characterized by the dynamical exponent $\vartheta = 1$ will generally be present in more complex acquisition schemes, such as multiple-wave-vector PG measurements whose lowest-order cumulant is completely determined by the time-dependent $D(t)$ (Jespersen, 2012). The corresponding higher-order cumulants, such as kurtosis, Eq. (E.4), will be also affected by the relatively slowly decaying $(lnt)/t^n$ terms as a result of disordered arrangement of axons in a bundle, again amplifying the role of extra-axonal water.

Conclusions

We showed that the long time behavior of diffusion coefficient transverse to a fiber bundle is determined by the disordered packing of the fibers. We identified short range disorder in the fibrous geometry in brain white matter, which may be a common feature of packings of biological building blocks.

As a consequence of the structural disorder, we predicted a charac teristically singular slow $(lnt)/t$ decrease of the diffusion coefficient transverse to the axons, Eq. (1). The logarithmic singularity (Eq. (1)) coming from extra-axonal space is shown to be more relevant than the $1/t$ decrease from water confined within axons, as $(lnt)/t$ eventually takes over the $1/t$ decrease. This may explain the strong bias in the values of apparent axonal diameters, especially on human scanners.

The unanticipated effect the random spatial arrangement of axons has on dMRI measurements, leads us to conclude that the time-dependent dMRI signal acquired transverse to a fiber tract at clinical diffusion weightings may be more sensitive to the extra-rather than to intra-axonal water, as well as to how randomly fibers are arranged within a bundle. This observation points at a crucial role of the mesoscopic effects which can be quantified using methods of condensed matter physics outlined here. Understanding this rich physics may open up exciting prospects of designing new imaging biomarkers of neuronal integrity based on changes of the geometry of extra-axonal space, such as axonal loss and demyelination, as a result of disease, aging, or normal development.

Supplementary Material

Refer to Web version on PubMed Central for supplementary material.

Acknowledgments

Appendix A. Relation of the diffusion coefficient to the structure correlation function

Knowledge of the structure correlator allows us to tie in long-time diffusion behavior with the disorder in a system via the homogenization argument, as introduced in Ref. Novikov et al. (2014). Briefly, this argument proceeds in two steps.

At the first step, one realizes that, no matter how strongly heteroge neous the system is microscopically, at long times these inhomogeneities become effectively coarse grained (homogenized) over the increasing diffusion length scale $L(t) = \left\langle [\delta x(t)]^2 \right\rangle^{1/2} \simeq \sqrt{2 D_\infty t}$, where D_∞ is the finite bulk diffusion coefficient and $\delta x = x(t) - x(0)$. In other words, while at short times the diffusing molecules "see" individual axonal walls and other sharp μm-level features, at longer times these features are progressively blurred, becoming indistinguishable, from the diffusion standpoint, from some effective, almost uniform medium. This looks as if a Gaussian filter with a window $\sim L(t) \gg \langle r_{ext} \rangle$ were applied to a medium. At this point, it is justifiable to introduce a coarse-grained local diffusion coefficient $D(r)$ which smoothly varies on the scale $L(t)$, and whose variation $\delta D(r) = D(r) - D_\infty$ becomes small, asymptotically approaching zero as $t \to \infty$. This smallness in turn justifies applying the lowest-order perturbation theory for the effective diffusivity in a medium with a weakly-varying local $D(r)$. Technically, this theory is most directly built in the frequency domain, for the dispersive diffusivity $D(\omega)$ (Ernst et al., 1984; Novikov and Kiselev, 2010; Novikov et al., 2014):

$$\mathscr{D}(\omega) \simeq D_\infty + \frac{-i\omega}{D_\infty d} \int \frac{d^d k}{(2\pi)^d} \frac{\Gamma_D(k)}{-i\omega + D_\infty k^2} \quad \text{(A.1)}$$

where $\Gamma_D(k) = \int \Gamma_D(r) e^{-ikr} d^d r$ is the Fourier transform of the two-point correlation function $\Gamma_D(r) = \langle \delta D(r_0 + r) \delta D(r_0) \rangle$ of the coarse-grained weakly-varying diffusion coefficient in d spatial dimensions. Here we con sider a statistically isotropic case, so that $\Gamma_D(k)$ depends only on $k = |k|$. In the time domain, Eq. (A.1) yields

$$D_{inst}(t) \simeq D_\infty + \frac{1}{D_\infty d} \int \frac{d^d k}{(2\pi)^d} \Gamma_D(k) e^{-D_\infty k^2 t}. \quad \text{(A.2)}$$

At the second step, one needs to relate a somewhat artificial object, Γ_D, entering Eqs. (A.1) and (A.2), to the correlation function $\Gamma(r) = \langle \rho(r_0 + r) \rho(r_0) \rangle$ of the actual restrictions, Eq. (B.1) above. As it has been realized in Ref. Novikov et al. (2014), in the long-distance (or low k) limit, these correlation functions become asymptotically proportional to each other:

$$\Gamma_D(k) \underset{k \to 0}{\simeq} C \cdot \Gamma(k), \quad C = \left(\frac{\partial D_\infty}{\partial \bar{\rho}} \right)^2. \quad \text{(A.3)}$$

The dependence $D_\infty \left(\bar{\rho} \right)$ of the macroscopic diffusion coefficient on r of the restrictions (e.g. axons) is the macroscopic density $\bar{\rho} = \langle \rho (\mathrm{r}) \rangle$ of the restrictions (e.g. axons) is non-singular, such that $0 < C < \infty$, as long as the system is not at its percolation transition, so that $D_\infty > 0$ in the extracellular space, which is always the case for neuronal tracts. Therefore, in a general situation, i.e. away from the singular packing density (for which $D_\infty = 0$), the $\omega \to 0$ and $t \to \infty$ asymptotic forms of Eqs. (A.1) and (A.2) can be (up to a coefficient C) deduced by plugging in the corresponding $k \to 0$ behavior of the structure correlator $\Gamma(k) \sim k^p$.

For the short-range disorder, p = 0, the correlation function $\Gamma(k)$ has a plateau $\Gamma(k)|_{k \to +0} > 0$ as $k \to 0$, Fig. 4; hence, a similar plateau $\Gamma_D(k)|_{k \to +0} = C \cdot \Gamma(k)|_{k \to +0}$ enters Eq. (A.1). Substituting this value into Eqs. (A.1) and (A.2) for $d = 2$, we obtain Eqs. (1), (2), (8), (18), and (19) with the coefficient

$$A = \frac{C \cdot \Gamma(k)|_{k \to +0}}{8\pi D_\infty^2}. \quad (A.4)$$

An accurate theory of the parameter A is nontrivial, as it involves finding analytically the dependence $D_\infty \left(\bar{\rho} \right)$, and is beyond the scope of this work. Here, we roughly estimate

$$A \sim \frac{\Gamma_D(k)|_{k \to +0}}{D_\infty^2} \sim \frac{var \{D(r)\} \cdot L_{\min}^2}{D_\infty^2} \sim \frac{D_\infty^2 \cdot l_c^2}{D_\infty^2} = t_c^2$$

based on the fact that, similar to the correlation function for the Poissonian disorder, $\Gamma_D(r)$ is dominated by a δ-function peak around r = 0 of amplitude $\sim var\{D(r)\} = \langle D^2(r) \rangle - \langle D(r) \rangle^2$ and width $L_{\min} \sim l_c$ corresponding to the minimal diffusion length scale at which we coarse-grained the medium and applied Eq. (A.1). This peak sharply decreases to 0 for $r \gg l_c$. Coarse-graining past l_c means that the fluctuations of $D(r)$ are already small, $var \{D(\mathrm{r})\} \lesssim D_\infty^2$. This estimate for A is in agreement with our data summarized in Table 2. The scaling $A \sim l_c^2$ (Supplementary fig. S4) is only approximate, since the plateau $\Gamma_D(k)|_{k \to +0}$ is determined not only by l_c but also by how strongly the objects "repel" each other, cf. Fig. 4 showing fairly strong sensitivity of the plateau value $\Gamma(k)|_{k \to +0}$ to the arrangement of the objects. Now it is also evident that the units for $\rho(r)$ in the examples of Fig. 3 (cf. Appendix B) are inessential, compensated by the respective units in the derivative in C, Eq. (A.3).

Appendix B. The structure correlation function Γ(k)

In order to formalize the qualitative difference between the computer-generated ordered packing in Panel a and the disordered ones in Panels b–d of Fig. 3, consider the density correlation function defined in a standard way,

$$\Gamma(r) = \langle \rho(r+r_0) \rho(r_0) \rangle_{r_0} \equiv \int \rho(r+r_0) \rho(r_0) \frac{dr_0}{V} \quad \text{(B.1)}$$

where $\rho(r)$ is the density of restrictions (black pixels in our examples in Fig. 3) at the point r, and V is the sample volume (area). The units of $\rho(r)$ and the overall normalization are not important for the qualitative distinction we are going to illustrate (cf. Appendix A); here we assumed $\rho = 1$ for the black pixels and $\rho = 0$ for the white pixels in Fig. 3.

Practically, the correlation functions of the restrictions in Fig. 4 are calculated in the Fourier domain, using the equivalence with the power spectral density

$$\Gamma(k) = \int e^{-ikr} \rho(r+r_0) \rho(r_0) \, dr \frac{dr_0}{V} \equiv \frac{1}{V} \rho(-k) \rho(k), \quad \text{(B.2)}$$

where $\rho(k) = \int dr \, e^{-ikr} \rho(r) = \rho^*(-k)$. In particular, given the shape functions, $v_j(r) = 1$ inside an object and 0 outside (cf. Fig. 3), we find $\rho(\mathbf{r}) = \sum_{j=1}^{N} v_j(r - r_j)$ for any array of shapes, with the Fourier transform given by

$$\rho(k) = \sum_{j=1}^{N} v_j(k) e^{-ikr_j}. \quad \text{(B.3)}$$

We note a few important properties of the function (Eq. (B.2)).

1. Large-k behavior For a disk of radius a, $v|_{r<a} = 1$, $v(k) = 2\pi a J_1(ka)/k$, where J_1 is a Bessel function of the first kind. We note that $v|_{ka\gg} - 3/2$. This scaling at large k is a general signature of the sharp boundaries with finite curvature in two dimensions, and is indeed present in Fig. 4 in the form $\Gamma(k) \sim |v(k)|^2 \sim k^{-3}$ as $k \to \infty$ both for the disks and for the randomly-shaped axons from Fig. 3d. 2. Normalization Consider the case of totally uncorrelated positions r_j of the objects (the Poissonian disorder), and let us also for simplicity assume them identical, $v_j \equiv v$ in Eq. (B.3). Substituting Eq. (B.3) in Eq. (B.2), we obtain

$$\Gamma_{Poiss}(k) = \frac{|v(k)|^2}{V} \sum_{j,j'=1}^{N} e^{ik\left(r_j - r_{j'}\right)} = n|v(k)|^2, \quad n = \frac{N}{V}, \quad \text{(47)}$$

since only the terms with $j = j'$ survive and the rest are averaged to zero due to the random phases. Hence, the plateau value for the Poissonian disorder is $\Gamma_{Poiss}(k)|_{k\to+0} = nv_0^2 \equiv \phi v_0$, where $v_0 = v(k)|_{k=0}$ is the volume (area) of a single object, and $\varphi = nv_0$ is the volume (area) fraction of the objects.

The Poissonian disorder is a good reference point, hence we have chosen to normalize all correlation functions in Fig. 4 onto , and the the value φv_0. For the axons in Fig. 3f, we defined $v_0 \equiv \varphi/n$ and the (external) object radius $\langle r_{ext} \rangle = \sqrt{v_0/\pi}$ for the k=axis normalization. We can see that the top curve, corresponding to Fig. 3d, plateaus at almost unity. (It does not reach unity because we assign $\rho = 1$ instead of $\rho = m$ to the pixels where m disks overlap, so there is a bit of anti-correlation baked in this $\rho(r)$.) Interestingly, all other correlation

functions have plateaus notably below φv_0, which is ex pected since the objects are anti-correlated due to their "repulsion" (non-overlap condition).

3. Discontinuity at $k = 0$ Since $\rho(k)|_{k=0} = V\varphi$, which is the volume (area) occupied by the objects, the value $\Gamma(k)|_{k=0} \equiv V\varphi^2$. This value is different from the plateau $\Gamma(k)|_{k \to +0}$ described above. This reflects the fact that $\Gamma(k)$ is discontinuous at $k = 0$. Physically, we are inter ested in the plateau $\Gamma(k)|_{k \to +0}$, as it reflects the statistical properties of the medium at distances $\sim 1/k$ which are large, but still smaller than the system size. Conversely, the value $\Gamma(k)|_{k=0}$ is irrelevant since it is only approached for k of the order of inverse system size (i.e. it is never approached in the thermodynamic limit N, $V \to \infty$), and thereby it cannot affect any observable physical quantities.

Appendix C. Time-dependent diffusion inside a perfectly reflecting cylinder in the narrow-pulse limit

The diffusion propagator for a perfectly reflecting cylinder of radius a is given by Stepišnik (1993) and Callaghan (1995)

$$
\begin{aligned}
S(t,q) = & \sum_{k=1}^{\infty} 4 e^{-\beta_{0k}^2 D_0 t/a^2} \frac{\left[(qa) J_0'(qa)\right]^2}{\left[(qa)^2 - \beta_{0k}^2\right]^2} \\
& + \sum_{n,k=1}^{\infty} 8 e^{-\beta_{nk}^2 D_0 t/a^2} \frac{\beta_{nk}^2}{\beta_{nk}^2 - n^2} \frac{\left[(qa) J_n'(qa)\right]^2}{\left[(qa)^2 - \beta_{nk}^2\right]^2}
\end{aligned} \quad \text{(C.1)}
$$

where J_n are Bessel functions of the first kind and β_{nk} is the kth root of their derivative $J_n'(x)$.

Taylor expanding up to q^2 reveals that only the Bessel functions J_n with $n = 0$ and 1 contribute at this level, as higher n result in the powers of q greater than 2. Similarly, the only k value needed for β_{0k} in the first sum is $k = 1$ with $\beta_{01} = 0$. Using $J_0(x) \simeq 1 - x^2/4 + x^4/64 - x^6/(36 \cdot 64)$ and $J_1(x) \simeq x/2$ for $x \ll 1$, Eq. (C.1) simplifies to

$$
\begin{aligned}
S(t,q) = & \ 1 - \frac{(qa)^2}{4} + \sum_{k=1}^{\infty} e^{-\beta_{1k}^2 D_0 t/a^2} \frac{2(qa)^2}{\beta_{1k}^2 (\beta_{1k}^2 - 1)} + \mathscr{O}\left(q^4\right) \\
\equiv & \ 1 - q^2 t D(t) + \mathscr{O}\left(q^4\right).
\end{aligned}
$$

From the above equation, we find

$$
D(t) = \frac{a^2}{4t} - \frac{2a^2}{t} \sum_{k=1}^{\infty} e^{-\beta_{1k}^2 D_0 t/a^2} \frac{1}{\beta_{1k}^2 (\beta_{1k}^2 - 1)}. \quad \text{(C.2)}
$$

This expression is plotted in Fig. C.1. Using (Neuman, 1974)

$$
\sum_{k=1}^{\infty} \frac{1}{\beta_{1k}^2 - 1} = \frac{1}{2}, \quad \sum_{k=1}^{\infty} \frac{1}{\beta_{1k}^2 (\beta_{1k}^2 - 1)} = \frac{1}{8}, \quad \text{(C.3)}
$$

the short-time limit of Eq. (C.2) is indeed $D(t)|_{t \to 0} = D_0$. The next-order correction, to which all the eigenmodes in Eq. (C.2) contribute, is the universal $-\sqrt{t}$ term (Mitra et al., 1992), shown in Fig. C.1. It works for $t \ll \tau_D$, where $\tau_D = a^2/D_0$ is the diffusion time for the cylinder. To see how all the eigenmodes contribute to the Mitra limit, one can substitute the summation by integration via approximating $\beta_{1k} \simeq \pi k$ for k >> 1, and regularize the resulting integral

$$\int_{\sim 1}^{\infty} \frac{\mathrm{d}k}{\pi^4 k^4} e^{-\pi^2 k^2 t/\tau_D} \simeq \frac{(t/\tau_D)^{3/2}}{2\pi} \Gamma\left(-\frac{3}{2}\right)$$

using Euler's Gamma function $\Gamma(-3/2) = 4\sqrt{\pi}/3$. (In the above equation, we extended the lower limit of integration to $k = 0$, with the understanding that there is no actual divergency at $k \to 0$ in the original discrete sum; the formally divergent integral $\int_0^{\infty} \mathrm{d}x\, x^{z-1} e^{-x}$ with $x = \pi^2 k^2 t/\tau_D$ is then understood in terms of the Gamma function $\Gamma(z)$ after analytic continuation in the complex plane of z from $z > 0$ to $z = -3/2$.) Collecting all the coefficients yields the exact Mitra $\sqrt{t}$ correction, with $S/V = 2\pi a/\pi a^2 = 2/a$, Fig. C.1.

In our example in Fig. C.1, we use $D_0 = 2\mu m^2/ms$ and a cylinder radius a = 0.5μm for a typical axon with an internal diameter of 1μm. For this case, $\tau_D = 0.13$ ms, therefore, for typical axonal length scales, all dMRI measurements will be in the long time limit. For the long times, the sum over the eigenmodes in Eq. (C.2) becomes negligible, and

$$D(t) \simeq \frac{a^2}{4t}, \quad t \gg \tau_D. \quad \text{(C.4)}$$

This limit is utilized in Eq. (27) of the main text.

From Eq. (C.2), using Eq. (4), we obtain the instantaneous

$$D_{inst}(t) = \sum_{k=1}^{\infty} \frac{2D_0}{\beta_{1k}^2 - 1} e^{-\beta_{1k}^2 D_0 t/a^2}. \quad \text{(C.5)}$$

Fig. C.1 shows how distinctly faster is the exponential decrease of $D_{inst}(t)$ (solid black line) as compared to the power law decrease (Eq. (C.4)). Indeed, practically, $D_{inst}(t)$ is already captured by the lowest $k = 1$ eigenmode in the sum (Eq. (C.5)), as shown by the dashed magenta line (cf. Eq. (9) of the main text). The higher modes are only really needed to get the correct $t \ll \tau_D$ behavior of Eqs. (C.2) and (C.5).

Appendix D. Frequency-dependent diffusion coefficient inside a perfectly reflecting cylinder

Taking the Fourier transform (Eq. (14)) of Eq. (C.5), we obtain

$$\mathscr{D}(\omega) = \sum_{k=1}^{\infty} \frac{2D_0}{\beta_{1k}^2 - 1} \cdot \frac{-i\omega}{\beta_{1k}^2 D_0/a^2 - i\omega}. \quad \text{(D.1)}$$

The lowest-order term in ω of Eq. (D.1) is purely imaginary, $\mathscr{D}(\omega) = -i\omega a^2/4 + \mathscr{O}(\omega^2)$, and corresponds to the long-time limit (C.4). The OG-measured real part of Eq. (D.1)

$$Re\,\mathscr{D}(\omega) = \sum_{k=1}^{\infty} \frac{2D_0}{\beta_{1k}^2 - 1} \cdot \frac{\omega^2}{\beta_{1k}^4 D_0^2/a^4 + \omega^2}. \quad \text{(D.2)}$$
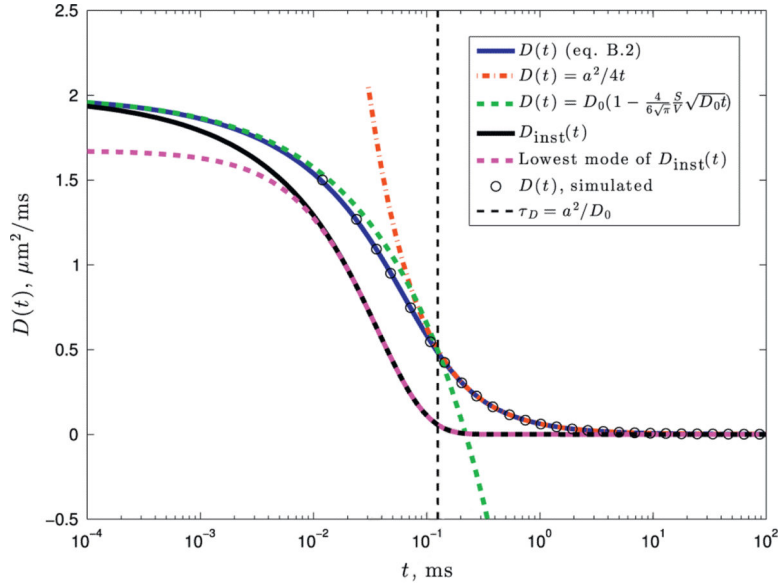

Fig. C.1.
Cumulative diffusion coefficient (Eq. (C.2)) for an impermeable cylinder for typical axonal parameters, $D_0 = 2\mu m^2/ms$ and radius $a = 0.5\mu m$. The characteristic diffusion time τ_D is shown by the vertical black dashed line. The diffusion times commonly employed in dMRI fall into the long time limit for typical axons. Note a much faster, exponential decrease of $D_{inst}(t)$ given by the first term of the sum (Eq. (C.5)) (dashed magenta), as compared to $\sim 1/t$ asymptote (Eq. (C.4)) of $D(t)$ (dot-dashed red). The MC simulated $D(t)$ (open circles) perfectly agrees with the theoretical value (C.2).

Its Taylor expansion around $\omega = 0$ starts from the ω^2 term. Using the relation (Neuman, 1974)

$$\sum_{k=1}^{\infty} \frac{2}{\beta_{1k}^4 (\beta_{1k}^2 - 1)} = \frac{7}{9} \approx 0.0729 \quad \text{(D.3)}$$

(note a misprint, 296 → 96 in Eq. (28) of that paper), we find

$$Re\,\mathscr{D}(\omega) = \frac{7}{96} \frac{a^4 \omega^2}{D_0} + \mathscr{O}(\omega^4). \quad \text{(D.4)}$$

The result (Eq. (D.2)), together with its low frequency limit (Eq. (D.4)), and its high frequency limit based on Ref. Novikov and Kiselev (2011) with $S/V = 2/a$, are plotted in Fig. D.1. We observe that for axons (generally, for impermeable cells) of ~ 1μm size, the high-

frequency limit is practically unattainable, as it requires frequencies beyond ~ 10 kHz, and the OG-measured diffusivity has a clear low-frequency parabolic dependence (Eq. (D.4)) within a few kHz range.

As with Eq. (C.5), we again see that the lowest $k = 1$ eigenmode very well captures the low-frequency behavior of ω . Indeed, the sums in Eqs. (C.3) and (D.3) converge very rapidly and are approximated their respective first terms involving only $\beta_{11} \approx 1.8412$. For instance, keeping only the k = 1 term in Eqs. (D.1)–(D.3), we get the ω^2 behavior with a coefficient $2/\left[\beta_{11}^4 \left(\beta_{11}^2 - 1\right)\right] \approx 0.0728$, approximating the exact coefficient in Eq. (D.4) within a 0.14% accuracy.

We note that a qualitatively similar dominance of the lowest eigen- mode also occurs for periodic lattices (Dunn and Bergman,1995; Sen et al., 1994; Sukstanskii et al., 2004; Novikov et al., 2014). The physical reason is the same: the spectrum of discrete eigenmodes, which, for sufficiently long $t \gg l_0^2/D_0$, where l_0 is the lattice constant, allows one to keep the lowest one, cf. Eq. (9), that is separated by a gap $\sim D_0/l_0^2$ from the rest, whose contributions exponentially die out even faster. This is the rationale behind the simple Lorentzian representation (Eq. (20)) used in the main text.

In disordered media, when there is no spectral gap, the sum (Eq. (A.2)) over the finite density of exponentially decaying eigenmodes yields a power law (Ernst et al., 1984; Machta et al., 1984; Visscher, 1984; Novikov et al., 2014). More generally, this is why transport properties of ordered and disordered systems are so qualitatively dis tinct, even at the level of purely classical diffusion, with this distinction becoming even more pronounced in the case of quantum transport, where disorder leads to localization of single-particle wave functions (Anderson, 1958; Abrahams et al., 1979).

Appendix E. Axonal diameter mapping up to O(q4) in the narrow-pulse limit

Consider first for simplicity the case of all axons to be of the same internal radius $r = a$, and the narrow pulse limit $\delta \ll t_c$ of diffusion weighting. The total signal is additive,

$$S(t, q) = f_{int} S_{int}(t, q) + f_{ext} S_{ext}(t, q), \quad q = g\delta, \quad \text{(E.1)}$$

where g is the diffusion-sensitizing gradient value (in the units of Larmor frequency per unit length) during the short pulse. We will now expand both terms of Eq. (E.1) up to $\mathscr{O}\left(q^4\right)$.

The intra-axonal signal in the limit t $\gg a^2/D_0$ is given by the $k = 1$ term in the first sum in Eq. (C.1). Its expansion

$$S_{int}(t, q) = 1 - \frac{(qa)^2}{4} + \frac{5 \cdot (qa)^4}{3 \cdot 64} + \mathscr{O}\left((qa)^6\right) \quad \text{(E.2)}$$

is equivalent to the kurtosis value $K_{int}|_{t \to \infty} = -1/2$ transverse to an impermeable cylinder. The cumulant expansion of the extra-axonal signal for $t \ll t_c$

$$lnS_{ext} \simeq - \left(D_\infty + Aln\frac{t}{t_c} \right) q^2 t + \frac{K_{ext}(t)}{6} \cdot \left(D_\infty q^2 t \right)^2 + \ldots \quad \text{(E.3)}$$

Using the approach (Novikov and Kiselev, 2010), we found (details to be published elsewhere) the kurtosis due to the disordered packing, as

$$\frac{K_{ext}(t)}{6} \simeq \frac{A}{D_\infty} \cdot \frac{ln\,(t/t_c)}{t}, \quad t \gg t_c. \quad \text{(E.4)}$$

One can already expect the behavior $K_{ext} \sim A/(D_\infty t)$ on purely dimensional grounds (kurtosis is dimensionless and must scale with the disorder strength $\sim A$). The lnt singularity is nontrivial and has the same origin as in Eq. (1). In Eq. (E.3), within the accuracy of keeping the terms $\sim Alnt$, we approximated $D(t)$ by D_∞ in the term $(D(t)q^2t)^2$. Substituting Eqs. (E.2) and (E.3) into Eq. (E.1) and regrouping the terms into the moments $\langle x^n \rangle$ of the total signal, we obtain

$$S = 1 - q^2 \left\langle x^2 \right\rangle /2! + q^4 \left\langle x^4 \right\rangle /4! + \mathcal{O}\left(q^6 \right), \quad \text{(E.5)}$$

$$\frac{\langle x^2 \rangle}{2!} = f_{int}\frac{a^2}{4} + f_{ext}\left(D_\infty t + Aln\frac{t}{t_c} \right), \quad \text{(E.6)}$$

$$\frac{\langle x^4 \rangle}{4!} = f_{int}\frac{5 \cdot a^4}{3 \cdot 64} + f_{ext}\left[\frac{K_{ext}}{6}(D_\infty t)^2 + \frac{1}{2}\left(D_\infty t + Aln\frac{t}{t_c} \right)^2 \right]. \quad \text{(E.7)}$$

Consider now the result of matching the q^2 and q^4 terms of Eq. (E.5) to those of the conventional model

$$S_0\left(t, q \right) = f_{int}S_{int}(t, q)\,|_{a \to r_{app}} + f_{ext}e^{-D_\infty q^2 t} \quad \text{(E.8)}$$

which assumes time-independent Gaussian diffusion in the extra-axonal space, with some apparent axonal radius r_{app} instead of a in the intra-axonal signal expansion (Eq. (E.2)).

Matching of $\langle x^2 \rangle$ terms of models in Eqs. (E.5) and (E.8) yields

$$f_{int} \cdot r_{app}^2 4 \equiv f_{int} \cdot a^2 4 + f_{ext} \cdot Aln\frac{t}{t_c}$$

which gives Eq. (34) after generalizing $a^2 \to \langle r^4 \rangle / \langle r^2 \rangle$ onto the distribution of the internal radii r by taking the volume average over the distribution of axons. Hence, fitting of the actual signal (Eq. (E.5)) to the conventional model (Eq. (E.8)) at the lowest diffusion weighting would give $r_{app}(t) > a$.
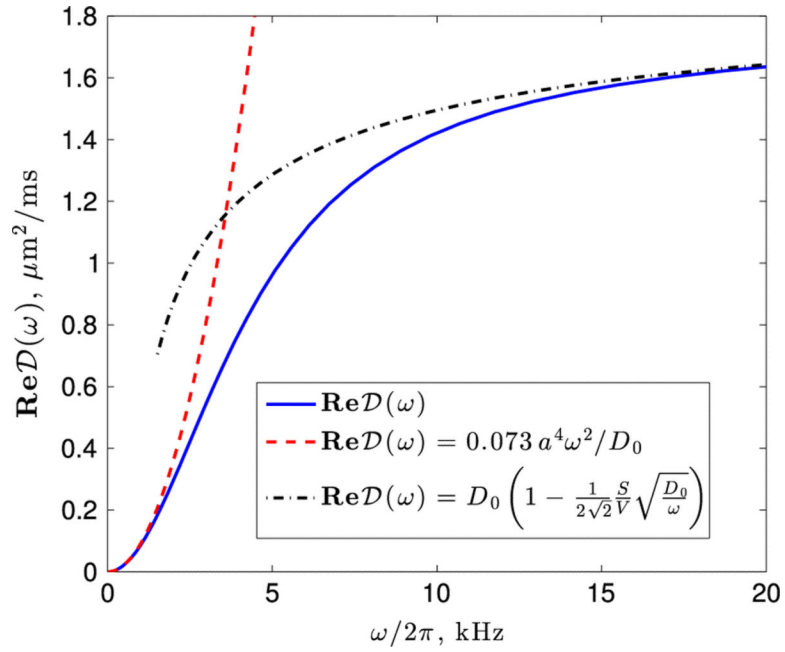
Fig. D.1.
Eq. (D.2) (solid blue line) plotted with $D_0 = 2\mu m^2$ /ms and a cylinder radius $a = 0.5\mu m$. Its low-frequency limit (Eq. (D.4)) and high-frequency limit are shown by the dashed red line and black dash-dotted lines, correspondingly.

The increase in the diffusion weighting would further bias the result for r_{app}. Matching of the $\langle x^4 \rangle$ terms,

$$f_{int}\frac{5 \cdot r_{app}^4}{3 \cdot 64} \equiv f_{int}\frac{5 \cdot a^4}{3 \cdot 64} + f_{ext}\left[\frac{K_{ext}}{6}(D_\infty t)^2 + D_\infty t \cdot A ln\frac{t}{t_c}\right]$$

where we neglected the $\sim A^2$ term as a small correction, yields a different expression for $r_{app}(t)$. Using Eq. (E.4), we find

$$r_{app}^4(t) \simeq a^4 + \frac{2 \cdot 3 \cdot 64}{5}\frac{f_{ext}}{f_{int}} \cdot A D_\infty t ln\frac{t}{t_c}, \quad t \gg t_c \quad \text{(E.9)}$$

where $a^4 \rightarrow \langle r^6 \rangle / \langle r^2 \rangle$ after averaging over the distribution of internal axonal radii. Eq. (E.9) is incompatible with Eq. (34) and requires $r_{app}(t)$ to increase even faster with t, as $(t ln t)^{1/4}$ instead of $(ln t)^{1/2}$ as $t \rightarrow \infty$. Hence, practically, increasing the sensitivity to the 4th-order cumulant with increasing diffusion weighting would bias the result (34) towards even greater values for r_{app}, leading to further overestimation of axonal radii.

Appendix F. Effects of finite exchange

In the main text, we considered a common assumption of negligible exchange in axonal tracts, $\tau_{ex} \gg t_{max}$, on the time scale t_{max} of the measurement (for OG, $t_{max} \sim \omega_{min}^{-1}$, where ω_{min} is the minimal OG fre quency). In this case, the two separate contributions to $D(\omega)$, $\sim$

$f_{ext}|\omega|$ (from the extra-axonal space due to the $p = 0$ disorder) and $\sim f_{int} \omega^2$ (from the confined water) add up, and the extra-axonal one dominates, cf. Eq. (31).

One may argue, however, that as fibers in the hippocampus are not highly myelinated, exchange may be notable, τ_{ex} t_{max}. We consider two limits: fast, $\tau_{ex} \ll t_c$ and slow, $\tau_{ex} > > t_c$.

If exchange is fast, $\tau_{ex} \ll t_c < t_{max}$, then by the time $t \sim \omega^{-1} \sim t_c$ our coarse-graining picture (Appendix A) becomes valid, the distinction between intra- and extra-axonal water already disappears. Namely, molecules travel both in and out of fibers many times, and collectively experience restrictions of the $p = 0$ universality class in $d = 2$. After ho mogenization over the diffusion length $L|_{t \sim 1/\omega} \gg l_c$, the coarse-grained $D(r)$ will have short range correlations with the same $l_c \sim 1\mu$ m, but now for all molecules, causing the $\sim |\omega|$ behavior. Certainly, the faster the exchange, the weaker the disorder and the smaller the amplitude A, Eq. (A.4), of the effect will be. In the limit of infinite permeability and equal diffusivities inside and outside fibers, the overall t and ω depen dence will disappear.

If exchange is slow, $t_c \ll \tau_{ex} < t_{max}$, the picture (Eq. (31)) of two unmixed compartments is only valid for $\omega > \tau_{ex}^{-1}$. We will now argue that the overall $D(\omega)$ will still be dominated by the $\omega|$ contribution for even smaller $\omega > \tau_{ex}^{-1}$, when the compartments become mixed. For these long times, we apply the coarse-grained Kärger description (Fieremans et al., 2010). In the $t \rightarrow \infty$, i.e. $\omega \rightarrow 0$ limit, it says that the overall diffusivity $D_\infty = f_{ext} D_\infty^{ext}$ does not depend on the exchange rate, and is given in terms of the extra-axonal tortuosity asymptote D_∞^{ext} calculated by setting exchange rate $\tau_{ex}^{-1} \rightarrow 0$. In our case, D_{ext} ω is not stationary; its residual dispersion originates as a result o coarse-graining (Appendix A) over the large diffusion length $L|_{t \sim 1/\omega} > \sqrt{D_\infty \tau_{ex}}$. We can now apply the argument (Fieremans et al., 2010) locally, within the domains of size $L|_{t \sim 1/\omega} \gg l_c$; each such domain's tortuosity limit $D(r) = f_{ext}(r) D^{ext}(r)$ is independent both of axonal diameters and of the exchange rate. Here, the local fraction $f_{ext}(r)$ and the extra-axonal diffusivity $D^{ext}(r)$ are the coarse-grained quantities for a given domain of size $L|_{t \sim 1/\omega}$ around the point r, and $D^{ext}(r)$ is calculated in the $\tau_{ex}^{-1} \rightarrow 0$ limit in accord with (Fieremans et al., 2010).

Assuming that spatial fluctuations of the local fraction $f_{ext}(r)$ are either short range or weaker, the correlation function $\Gamma_D(r)$ of the resulting $D(r)$ will have a $k \rightarrow 0$ plateau similar to that in the $\tau_{ex}^{-1} \rightarrow 0$ case, hence Eq. (A.1) yields similar $\sim |\omega|$ correction to D_∞ independent of the axonal diameters. In other words, when exchange is slow, $\tau_{ex} \gg t_c$, the overall diffusivity $D(\omega)$ should qualitatively behave as that in the no-exchange limit considered above, in agreement with Fig. 10.

As a result, the homogenization picture (Novikov et al., 2014) applies irrespective of the exchange, such that the overall behavior (Eq. (2)) remains valid, and the overall $D(\omega)$ is determined by the short range disordered packing, making the internal axonal diameters unobservable in the long time limit.

References

Abrahams E, Anderson PW, Licciardello DC, Ramakrishnan TV. Scaling theory of localization: absence of quantum diffusion in two dimensions. Phys. Rev. Lett. Mar.1979 42:673–676.

Aggarwal M, Jones MV, Calabresi PA, Mori S, Zhang J. Probing mouse brain microstructure using oscillating gradient diffusion MRI. Magn. Reson. Med. Jan; 2012 67(1):98–109. [PubMed: 21590726]

Alexander D, Hubbard P, Hall M, Moore E, Ptito M, Parker G, Dyrby T. Orientationally invariant indices of axon diameter and density from diffusion MRI. NeuroImage. 2010; 52:1374–1389. [PubMed: 20580932]

Anderson PW. Absence of diffusion in certain random lattices. Phys. Rev. 1958; 109:1492–1505.

Assaf Y, Blumenfeld-Katzir T, Yovel Y, Basser P. AxCaliber: a method for measuring axon diameter distribution from diffusion MRI. Magn. Reson. Med. Jun.2008 59(6):1347–1354. [PubMed: 18506799]

Barazany D, Basser P, Assaf Y. In vivo measurement of axon diameter distribution in the corpus callosum of rat brain. Brain. 2009; 132:1210–1220. [PubMed: 19403788]

Baron CA, Beaulieu C. Oscillating gradient spin-echo (ogse) diffusion tensor imaging of the human brain. Magn. Reson. Med. Oct.2013

Basser P, Mattiello J, LeBihan D. Estimation of the effective self-diffusion tensor from the NMR spin-echo. J. Magn. Reson. Ser. B. 1994; 103:247–254. [PubMed: 8019776]

Beaulieu C. The basis of anisotropic water diffusion in the nervous system — a technical review. NMR Biomed. 2002; 15:435–455. [PubMed: 12489094]

Bouchaud J-P, Georges A. Anomalous diffusion in disordered media — statistical mechanisms, models and physical applications. Phys. Rep. Rev. Sect. Phys. Lett. Nov; 1990 195(4–5):127–293.

Burcaw LM, Veraart J, Novikov DS, Fieremans E. In vivo observation of time-dependent diffusion in white matter in humans. Proc. Int. Soc. Magn. Reson. Med. 2014; 22:4434.

Callaghan P. Wall relaxation in pulsed-gradient spin echoes. J. Magn. Reson. Ser. A. 1995; 113:53–59.

Callaghan P, Eccles C, Xia Y. NMR microscopy of dynamic displacements: k-space and q-space imaging. J. Phys. E Sci. Instrum. 1988; 21:820–822.

Callaghan, PT. Principles of Nuclear Magnetic Resonance Microscopy. Clarendon; Oxford: 1991.

Dhital B, Leupold J, Kiselev VG. PFG filter for oscillating gradient diffusion measurements. Proc. Int. Soc. Magn. Reson. Med. 2014; 22:795.

Does M, Parsons E, Gore J. Oscillating gradient measurements of water diffusion in normal and globally ischemic rat brain. Magn. Reson. Med. 2003; 49:206–215. [PubMed: 12541239]

Donev A, Stillinger FH, Torquato S. Unexpected density fluctuations in jammed disordered sphere packings. Phys. Rev. Lett. Aug.2005a 95(9):090604. [PubMed: 16197201]

Donev A, Torquato S, Stillinger F. Neighbor list collision-driven molecular dynamics simulation for nonspherical hard particles. I. Algorithmic details. J. Comput. Phys. 2005b; 202:737–764.

Donev A, Torquato S, Stillinger F. Neighbor list collision-driven molecular dynamics simulation for nonspherical hard particles. II. Applications to ellipses and ellipsoids. J. Comput. Phys. 2005c; 202:765–793.

Dunn K-J, Bergman DJ. Self diffusion of nuclear spins in a porous medium with a periodic microstructure. J. Chem. Phys. 1995; 102(8):3041–3054.

Dyrby TB, Søgaard LV, Hall MG, Ptito M, Alexander DC. Contrast and stability of the axon diameter index from microstructure imaging with diffusion MRI. Magn. Reson. Med. Sep.2012

Ernst M, Machta J, Dorfman J, van Beijeren H. Long-time tails in stationary random-media. I. Theory. J. Stat. Phys. 1984; 34:477–495.

Fieremans E. The design of anisotropic diffusion phantoms for the validation of diffusion weighted magnetic resonance imaging. Phys. Med. Biol. 2008; 53:5405–5419. [PubMed: 18765890]

Fieremans E, De Deene Y, Delputte S, Ozdemir MS, D'Asseler Y, Vlassenbroeck J, Deblaere K, Achten E, Lemahieu I. Simulation and experimental verification of the diffusion in an anisotropic fiber phantom. J. Magn. Reson. Feb.2008 190(2):189–199. [PubMed: 18023218]

Fieremans E, Jensen JH, Helpern JA, Kim S, Grossman RI, Inglese M, Novikov DS. Diffusion distinguishes between axonal loss and demyelination in brain white matter. Proc. Int. Soc. Magn. Reson. Med. 2012; 20:714.

Fieremans E, Novikov DS, Jensen JH, Helpern JA. Monte Carlo study of a two-compartment exchange model of diffusion. NMR Biomed. 2010; 23:711–724. [PubMed: 20882537]

Grebenkov DS. NMR survey of reflected Brownian motion. Rev. Mod. Phys. Aug.2007 79:1077–1137.

Horowitz A, Barazany D, Tavor I, Bernstein M, Yovel G, Assaf Y. In vivo correlation between axon diameter and conduction velocity in the human brain. Brain Struct. Funct. Aug.2014

Horsfield M, Barker G, Mcdonald W. Self-diffusion in CNS tissue by volume-selective proton NMR. Magn. Reson. Med. 1994; 31:637–644. [PubMed: 8057816]

Huang SY, Nummenmaa A, Witzel T, Duval T, Cohen-Adad J, Wald LL, McNab JA. The impact of gradient strength on in vivo diffusion MRI estimates of axon diameter. NeuroImage. Feb.2015 106:464–472. [PubMed: 25498429]

Jespersen SN. Equivalence of double and single wave vector diffusion contrast at low diffusion weighting. NMR Biomed. Jun; 2012 25(6):813–818. [PubMed: 22134913]

Jespersen SN, Bjarkam CR, Nyengaard JR, Chakravarty MM, Hansen B, Vosegaard T, Ostergaard L, Yablonskiy D, Nielsen NC, Vestergaard-Poulsen P. Neurite density from magnetic resonance diffusion measurements at ultrahigh field: comparison with light microscopy and electron microscopy. NeuroImage. Jan; 2010 49(1):205–216. [PubMed: 19732836]

Jespersen SN, Kroenke CD, Ostergaard L, Ackerman JJH, Yablonskiy DA. Modeling dendrite density from magnetic resonance diffusion measurements. NeuroImage. Feb.2007 34(4):1473–1486. [PubMed: 17188901]

Kamenev, A. Field Theory of Non-Equilibrium Systems. Cambridge University Press; New York: 2011.

Kershaw J, Leuze C, Aoki I, Obata T, Kanno I, Ito H, Yamaguchi Y, Handa H. Systematic changes to the apparent diffusion tensor of in vivo rat brain measured with an oscillating-gradient spin-echo sequence. NeuroImage. Apr.2013 70:10–20. [PubMed: 23274188]

Kiselev, VG. Diffusion MRI: theory, methods and applications.. In: Jones, DK., editor. Ch. 10. The Cumulant Expansion: an Overarching Mathematical Framework for Understanding Diffusion NMR. Oxford University Press; New York: 2010.

Kunz N, Sizonenko SV, Hüppi PS, Gruetter R, van de Looij Y. Investigation of field and diffusion time dependence of the diffusion-weighted signal at ultrahigh magnetic fields. NMR Biomed. Oct; 2013 26(10):1251–1257. [PubMed: 23533088]

Lamantia A, Rakic P. Cytological and quantitative characteristics of 4 cerebral commissures in the rhesus monkey. J. Comp. Neurol. 1990; 291:520–537. [PubMed: 2329189]

Lee H-H, Burcaw LM, Veraart J, Fieremans E, Novikov DS. Low-pass filter effect of finite gradient duration on time-dependent diffusion in the human brain. Proc. Int. Soc. Magn. Reson. Med. 2015; 23:2777.

Lifshitz I. Energy spectrum of disordered systems. Adv. Phys. 1964; 13(52):483–536.

Machta J, Ernst M, van Beijeren H, Dorfman J. Long time tails in stationary random media II: applications. J. Stat. Phys. 1984; 35(3–4):413–442.

Mitra P, Sen P, Schwartz L, Le Doussal P. Diffusion propagator as a probe of the structure of porous media. Phys. Rev. Lett. 1992; 68:3555–3558. [PubMed: 10045734]

Mott, NF.; Davies, EA. Electronic Processes in Non-crystalline Materials. Oxford University Press; New York: 1971.

Neuman CH. Spin echo of spins diffusing in a bounded medium. J. Chem. Phys. Jun; 1974 60(11):4508–4511.

Novikov DS, Fieremans E. Relating extracellular diffusivity to cell size distribution and packing density as applied to white matter. Proc. Int. Soc. Magn. Reson. Med. 2012; 20:1829.

Novikov DS, Jensen JH, Helpern JA, Fieremans E. Revealing mesoscopic structural universality with diffusion. Proc. Natl. Acad. Sci. U. S. A. Apr; 2014 111(14):5088–5093. [PubMed: 24706873]

Novikov DS, Kiselev VG. Effective medium theory of a diffusion-weighted signal. NMR Biomed. 2010; 23:682–697. [PubMed: 20886563]

Novikov DS, Kiselev VG. Surface-to-volume ratio with oscillating gradients. J. Magn. Reson. 2011; 210:141–145. [PubMed: 21393035]

Panagiotaki E, Schneider T, Siow B, Hall MG, Lythgoe MF, Alexander DC. Compartment models of the diffusion MR signal in brain white matter: a taxonomy and comparison. NeuroImage. Feb; 2012 59(3):2241–2254. [PubMed: 22001791]

Portnoy S, Flint J, Blackband S, Stanisz G. Oscillating and pulsed gradient diffusion magnetic resonance microscopy over an extended b-value range: implications for the characterization of tissue microstructure. Magn. Reson. Med. 2013; 69:1131–1145. [PubMed: 22576352]

Pyatigorskaya N, Le Bihan D, Reynaud O, Ciobanu L. Relationship between the diffusion time and the diffusion MRI signal observed at 17.2 tesla in the healthy rat brain cortex. Magn. Reson. Med. Sep.2013

Rushton W. A theory of the effects of fibre size in medullated nerve. J. Physiol. Sep; 1951 115(1): 101–122. [PubMed: 14889433]

Savitzky A, Golay M. Smoothing and differentiation of data by simplified least squares procedures. Anal. Chem. 1964; 36:1627–1639.

Sen PN, Schwartz LM, Mitra PP, Halperin BI. Surface relaxation and the long-time diffusion coefficient in porous media: periodic geometries. Phys. Rev. B. Jan.1994 49:215–225.

Shklovskii, BI.; Efros, AL. Electronic Properties of Doped Semiconductors. Springer; Heidelberg: 1984.

Stepisnik J, Lasic S, Mohoric A, Sersa I, Sepe A. Velocity autocorrelation spectra of fluid in porous media measured by the CPMG sequence and constant magnetic field gradient. Magn. Reson. Imaging. May; 2007 25(4):517–520. [PubMed: 17466777]

Stepišnik J. Time-dependent self-diffusion by NMR spin-echo. Physica B. 1993; 183:343–350.

Sukstanskii AL, Yablonskiy DA, Ackerman JJH. Effects of permeable boundaries on the diffusion-attenuated MR signal: insights from a one-dimensional model. J. Magn. Reson. Sep.2004 170(1): 56–66. [PubMed: 15324758]

Szafer A, Zhong J, Gore JC. Theoretical model for water diffusion in tissues. Magn. Reson. Med. May; 1995 33(5):697–712. [PubMed: 7596275]

Tofts P, Lloyd D, Clark C, Barker G, Parker G, McConville P, Baldock C, Pope J. Test liquids for quantitative MRI measurements of self-diffusion coefficient in vivo. Magn. Reson. Med. Mar. 2000 43(3):368–374. [PubMed: 10725879]

Torquato S, Stillinger FH. Local density fluctuations, hyperuniformity, and order metrics (Vol E 68, Art No 041113, 2003). Phys. Rev. E. Dec.2003 68(6):069901.

Van AT, Holdsworth SJ, Bammer R. In vivo investigation of restricted diffusion in the human brain with optimized oscillating diffusion gradient encoding. Magn. Reson. Med. Jan; 2014 71(1):83–94. [PubMed: 23447055]

Visscher PB. Analytic fixed points of discrete equations of motion: universality in homogeneous diffusive systems. Phys. Rev. B. 1984; 29:5462–5471.

Xu J, Li H, Harkins KD, Jiang X, Xie J, Kang H, Does MD, Gore JC. Mapping mean axon diameter and axonal volume fraction by MRI using temporal diffusion spectroscopy. NeuroImage. Dec. 2014 103:10–19. [PubMed: 25225002]

Zhang H, Hubbard P, Parker G, Alexander D. Axon diameter mapping in the presence of orientation dispersion with diffusion MRI. NeuroImage. 2011; 56:1301–1315. [PubMed: 21316474]

Zurek M, Winters K, Zhang J, Rodriguez J, Novikov DS, Kim S, Fieremans E. Assessment of white matter tract integrity metrics in cuprizone-induced white matter degeneration with diffusion MRI. Proc. ISMRM. 2014; 22:2685.
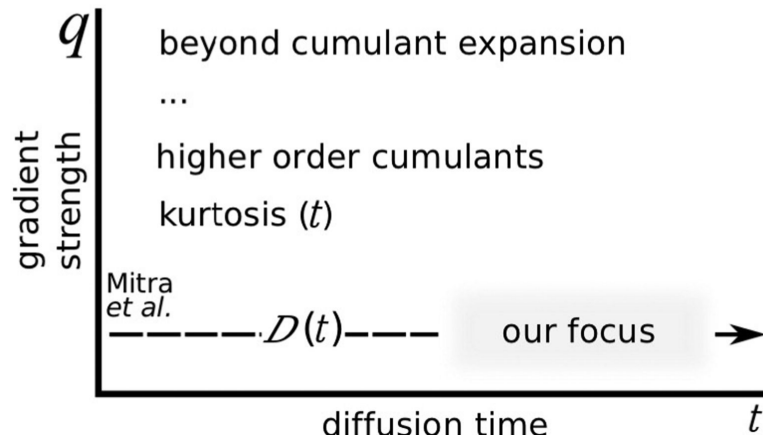
Fig. 1.
Parameter space of diffusion MRI is two-dimensional: by increasing q one accesses the progressively higher-order diffusion cumulants $\langle(\delta x)^2\rangle$, $\langle(\delta x)^4\rangle - 3\langle(\delta x)^2\rangle^2$, ... (Kiselev, 2010), whereas the dependence along the t-axis reflects their evolution over an increasing diffusion length scale $\sim \sqrt{tD(t)}$. Our focus is on $D(t) = \langle(\delta x)^2\rangle/2t$ for accessible (i.e. long) diffusion time t.
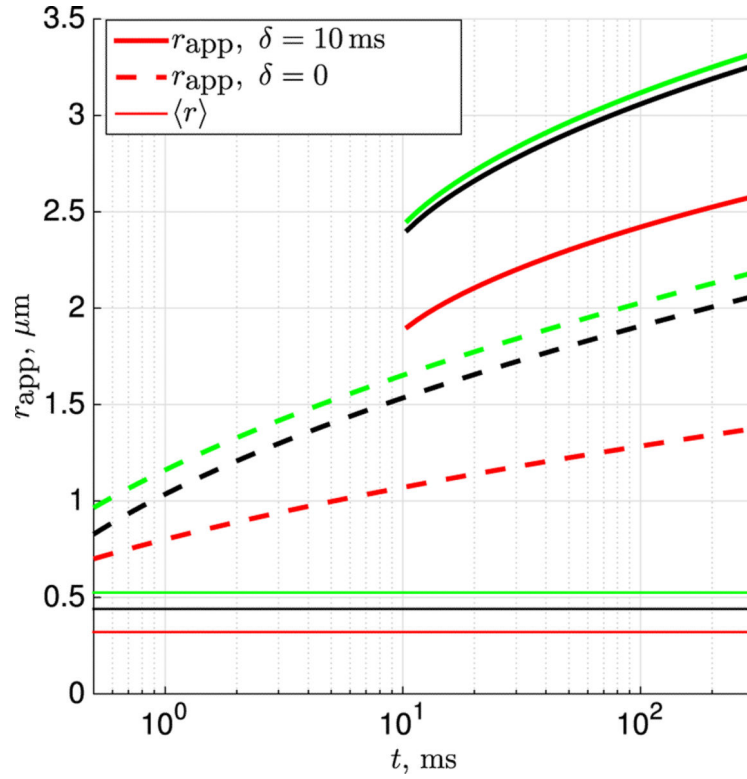
Fig. 2.
Apparent axonal radius $r_{\text{app}}(t)$ for rhesus monkey corpus callosum sectors 2, 4, 6 (red, black and green), obtained from MC-simulated overall diffusion coefficient $D(t)$ in the narrow-pulse limit (dashed) and with pulse width $\delta = 10$ ms (derived from MC data, with diffusion time $t \equiv \quad \delta$), by attributing all time dependence to the intra-axonal water. [Results apply for regions I and II of the phase diagram, cf. Discussion, Fig. 12; see Eqs. (34) and (39), and Table 3.] Note that $r_{\text{app}}(t)$ greatly exceeds the corresponding mean radius $\langle r \rangle$ (thin lines); for $\delta = 10$ ms the extra-axonal contribution is completely dominant. Singularity ((1)) is reflected in $r_{app}^2 \sim lnt, \delta = 0; r_{app}^4 \sim lnt, \delta > t_c$.
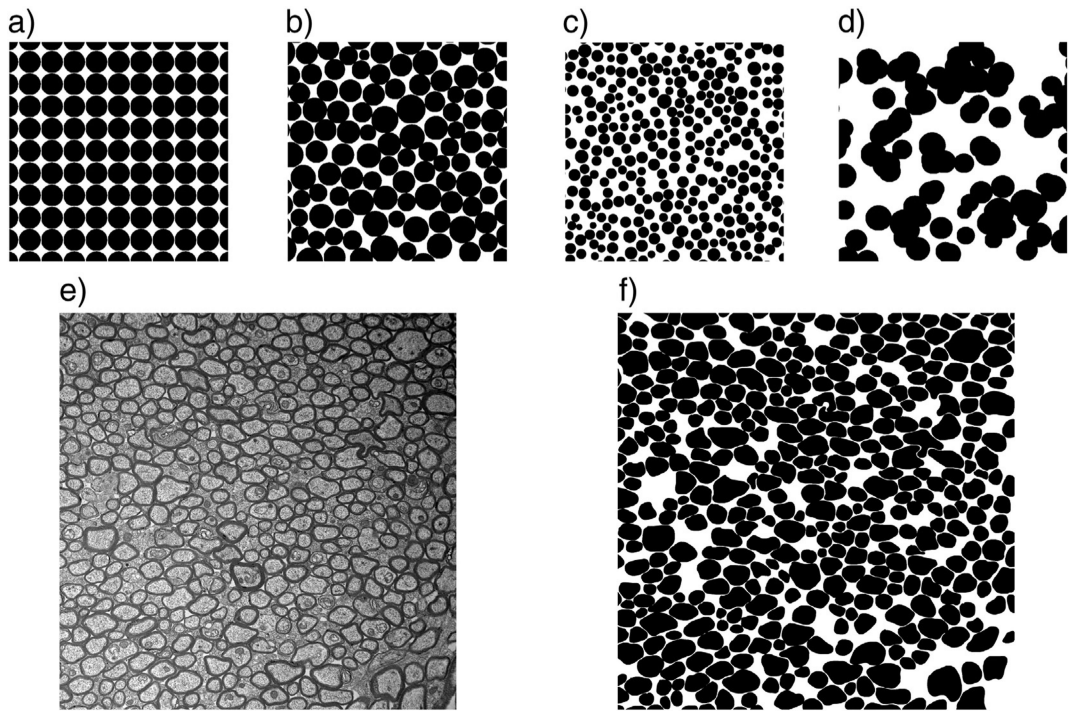
Fig. 3.
Examples of 2d packings, relevant for the extra-axonal diffusion transverse to fibers, with their correlation functions shown in Fig. 4. a, Order: a square lattice of disks. b, Random non-overlapping packing of disks with a volume fraction $\varphi = 0.75$. c, The same as for b, but with a volume fraction $\varphi = 0.5$. Note the disks have the same distribution of radii as in b, but we show a larger subset of the full packing. d, Random disk pack where disks are allowed to freely overlap (Poissonian disorder), $\varphi = 0.55$. e, Electron microscope image of the splenium of a 20 week old female C57BL16 mouse (Zurek et al., 2014). f, Axons from e, including myelin, outlined by hand, with calculated volume fraction $\varphi = 0.7$, exemplifying restrictions to diffusion in extra-axonal space.
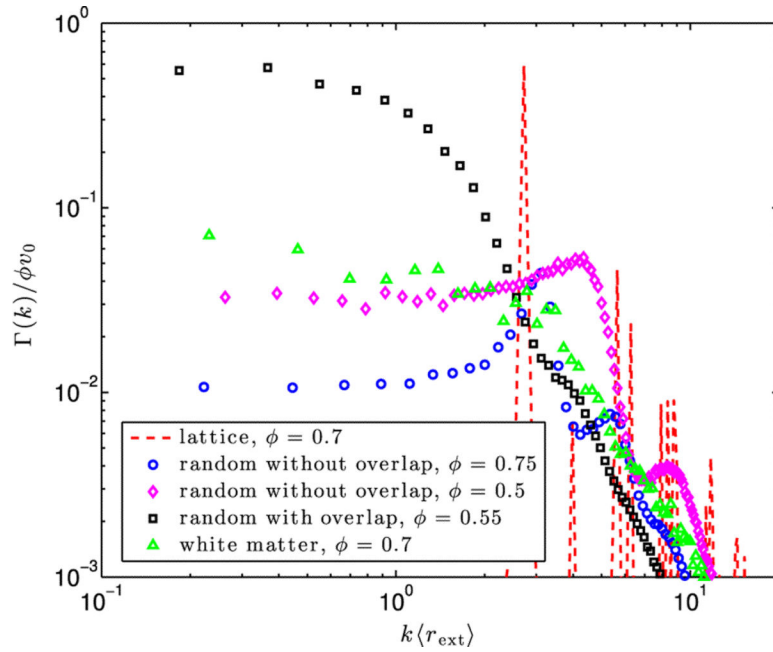
Fig. 4.

Angular-averaged Fourier transform $\Gamma(k)$ of the normalized density correlation function (B. 1) equivalently, power spectrum, Eq. (B.2) for the five structures shown in Fig. 3, as function of radial k, which is made dimensionless by multiplying by the average object radius $\langle r_{\text{ext}}\rangle$ for each packing (cf. Appendix B). Square lattice of disks (dashed red line), Fig. 3a, exhibits Bragg peaks, such that $\Gamma(k) \equiv 0$ for k below the first peak, corresponding to exponent $p = \infty$. Randomly placed disks without overlap with a volume fraction $\varphi = 0.75$ (blue), Fig. 3b; $\varphi = 0.5$ (magenta), Fig. 3c; and with overlap (black), Fig. 3d, exhibit short-range correlations, with the finite plateau $\Gamma(k)|_{k \to +0} = \text{const} > 0$, corresponding to exponent $p = 0$. As expected by how they are packed, these arrangements are progressively more disordered, consistent with an increase in the plateau value $\Gamma(k)|_{k \to +0}$. The density correlator for axons, Fig. 3f, with $\varphi = 0.7$, seems to approach a finite plateau $\Gamma(k)|_{k \to +0}$, corresponding to the exponent (Eq. (10)). The plateau value is roughly that of the randomly packed disks with $\varphi = 0.5$, indicating a fairly disordered arrangement. For all packings, the disorder correlation length $l_c \sim 1/k_c \sim \langle r_{ext}\rangle$. The overall $1/k^3$ decrease at large k for all curves is due to the 2d curved boundaries (see Appendix B), a short-scale signature of the individual objects that is not relevant for the long-time behavior of diffusion.
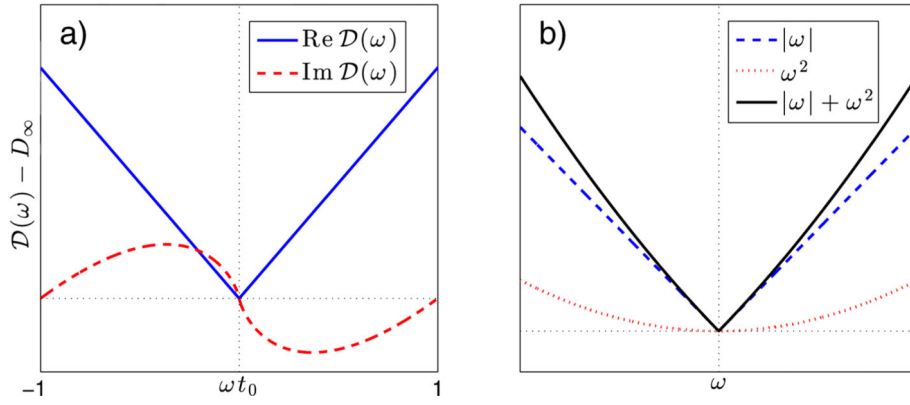
Fig. 5.

a, The real (solid blue line) and imaginary (dashed red line) parts of $D(\omega)$. Note that $ReD(\omega)$ is an even function, which requires even powers of ω in its Taylor expansion, in case it is analytic around $\omega = 0$. By this token, an OG-measured linear-in-frequency behavior of $ReD(\omega)$ signifies the non-analytic behavior (Eq. (19)) for the full $D(\omega)$, involving the modulus $|\omega|$ rather than ω for $ReD(\omega)$ to remain even. b, A graphical representation of Eq. (31). At low ω, the singular (non-analytic) $|\omega|$ term, which is a signature of short-range disorder, will dominate the regular (analytic) ω^2 contribution to $D(\omega)$.
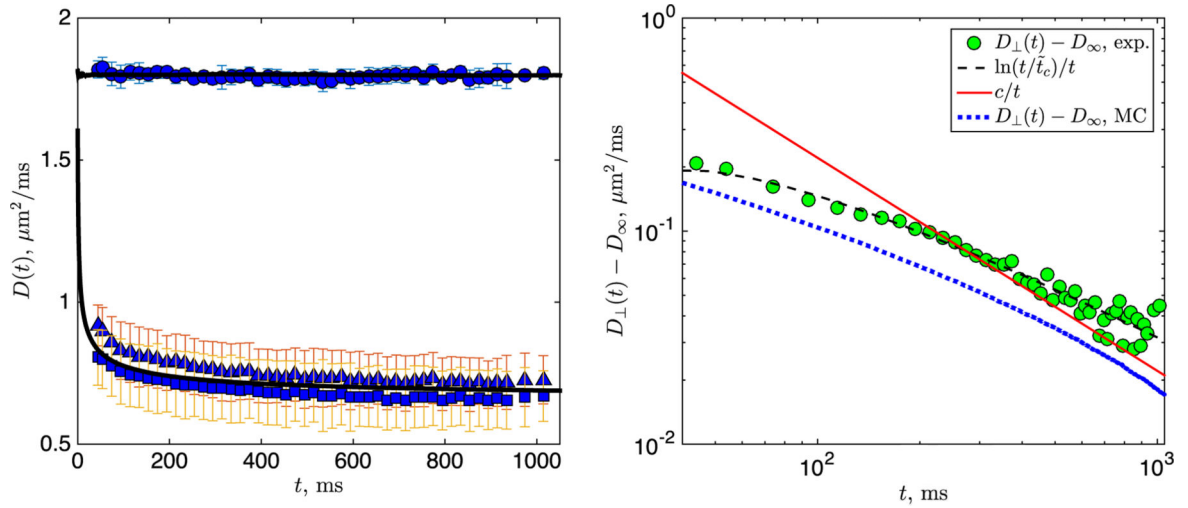
Fig. 6.
a, Diffusion tensor eigenvalues $\lambda_1 > \lambda_2 > \lambda_3$ as measured in the phantom, as a function of diffusion time, t. MC data is shown by the solid black line. b, The difference $D_\perp(t) - D_\infty$, where $D_\perp(t)$ is given by Eq. (30). Two fits are shown: $ln(t/t_c)/t$ (black dashed line) and c/t (red solid line). The MC data is also plotted (dotted blue line) for comparison. The mismatch from experiment, amplified by the log scale, is likely due to both imperfect subtraction of D_∞ and unknown details of packing geometry in the fiber phantom. The slope of the curves slowly increases with t, approaching the value -1 of the red line, indicative of the behavior (Eq. (1)). As axons are ~10 times thinner than the Dyneema fibers, our range of t corresponds to ~100 times shorter time scale for the brain, t 10 ms, cf. Fig. 11 below.
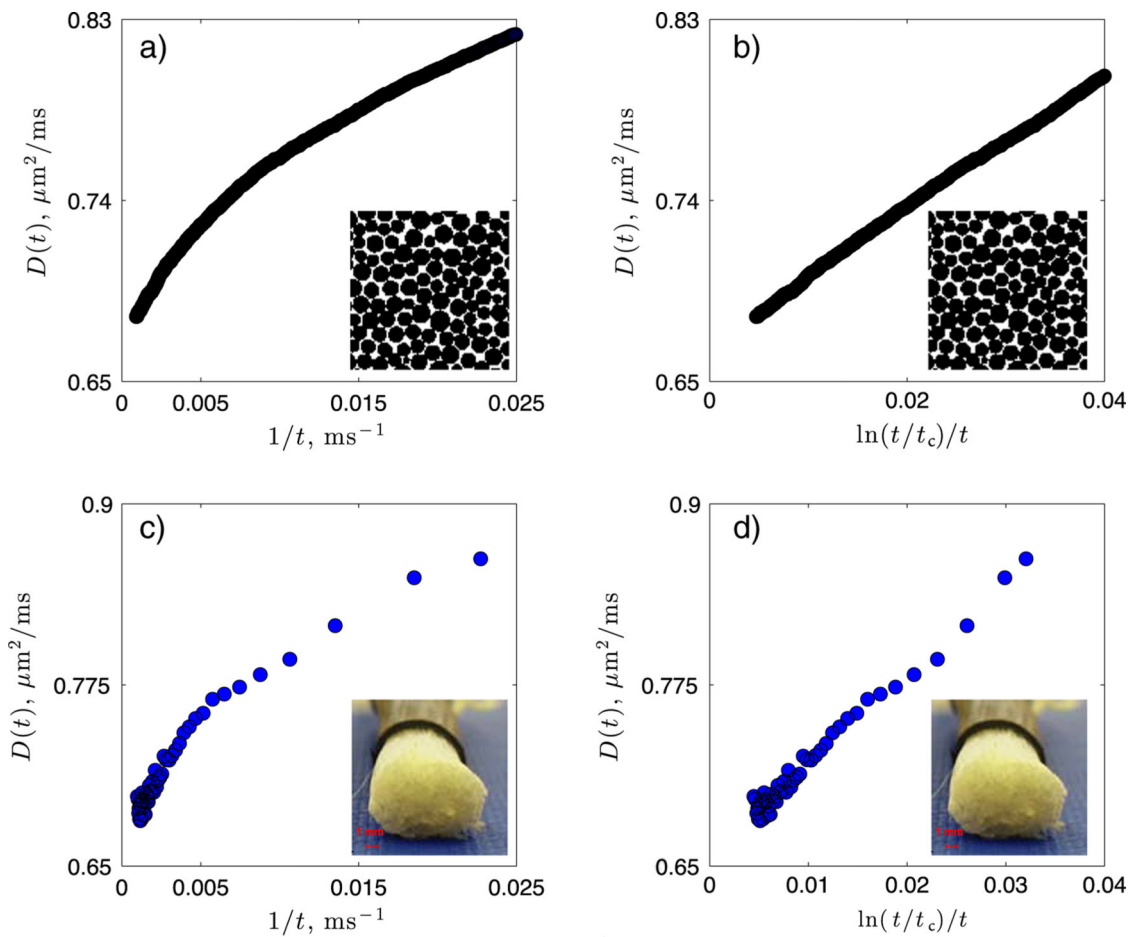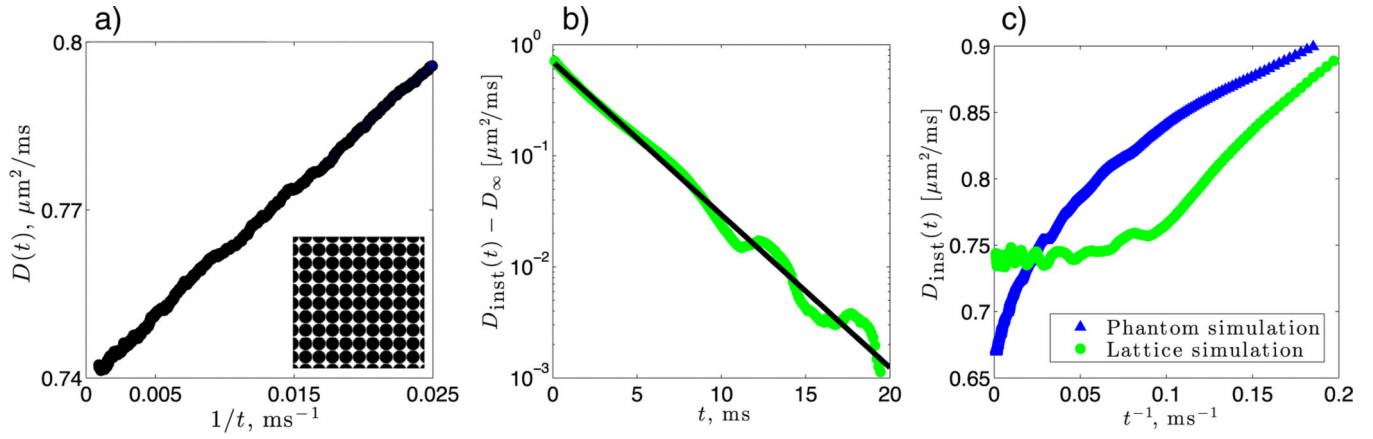
Fig. 7.
Identifying the logarithmic singularity Eq. (1) in the cumulative diffusion coefficient $D(t)$, cf. Eq. (3), for the randomly packed fibers. a, MC-simulated $D(t)$ plotted as function of $1/t$ for diffusion in the exterior of a random disk packing (fragment shown in Fig. 3b). The logarithmic singularity is manifest in the "bend". b, This "bend" straightens up when $D(t)$ is replotted with respect to $ln(t/t_c)/t$. c, d: The same as for a and b, but with experimental $D_\perp(t)$, Eq. (30) and Fig. 6, transverse to the fiber phantom.

Fig. 8.
Effects of the periodic geometry. a, $D(t)$ for MC simulated diffusion in the exterior of periodically ordered disks. Note the absence of the "bend" (cf. Fig. 7), illustrating that the logarithmic singularity is absent in an ordered medium. b, $D_{inst}(t)$ derived from the same simulated data, and plotted on a semilog plot, indicating an exponentially fast approach of D_∞. A fit to const e^{-t/t_0} is shown by the black line. c, The qualitatively different approach to D_∞ of MC-derived $D_{inst}(t)$ for the periodic (green) and randomly packed disks (blue). While $D_{inst}(t)$ for the regular lattice of disks reaches its D_∞ very rapidly (within about 10 ms), the blue curve (mimicking a randomly packed fiber phantom) slowly straightens out, as $t^{-1} \rightarrow 0$, cf. Fig. 9b for the magnified time domain 100 ms $< \sim t$ 1000 ms.
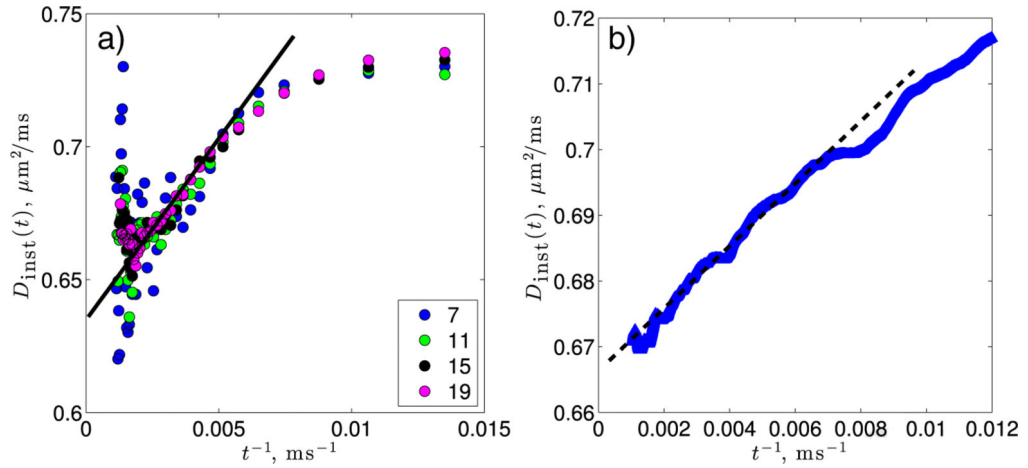
Fig. 9.
Identifying the dynamical exponent ϑ in the instantaneous diffusion coefficient $D_{\text{inst}}(t)$, Eq. (5): a, in experiment on a fiber phantom; b, in MC simulated diffusion in a random disk packing. For a, different symbols correspond to Savitzky–Golay smoothing windows of width indicated in the legend. For b, the window is up to 2001 MC time points. a, The solid black line indicates the linear dependence on $1/t$ at long times, indicative of the exponents $\vartheta = 1$ and $p = 0$. b, The long time limit of the simulated random pack shows a linear dependence on $1/t$ (dashed line) similar to that of our experimental data in a. Both curves display asymptotic $1/t$ dependence when $D_{\text{inst}}(t)$ is within about 10% of $D\infty$ (the extrapolated intercept at $t^{-1} \to 0$), for the times $t \quad 100$ ms. This would correspond to $t \quad 1$ ms for the axons, cf. Fig. 11.
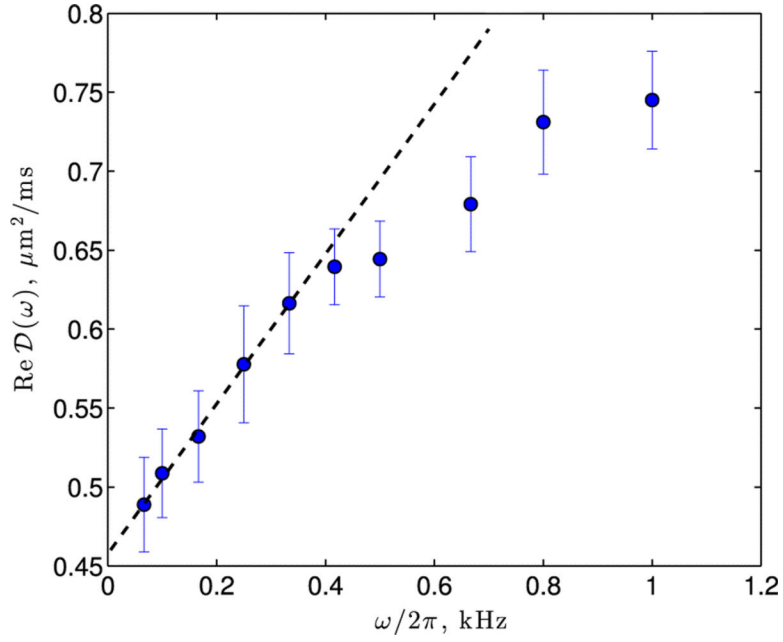
Fig. 10.
OG data from Fig. 6a of Portnoy et al. (2013). The dashed black line is the guide to the eye indicating the linear frequency dependence at small ω, corresponding to the long diffusion times. No trace of the "parabolic" $\sim \omega^2$ dependence from water confined within fibers is seen, in agreement with our argument in Eq. (31) and Fig. 5b, suggesting that the dispersion of $D(\omega)$ is dominated by the extra-axonal water with the dynamical exponent $\vartheta = 1$, Eq. (11). This yields the structural exponent p = 0, Eq. (10), confirming the short-range disorder in packing seen in histology, cf. Figs. 3f and 4.
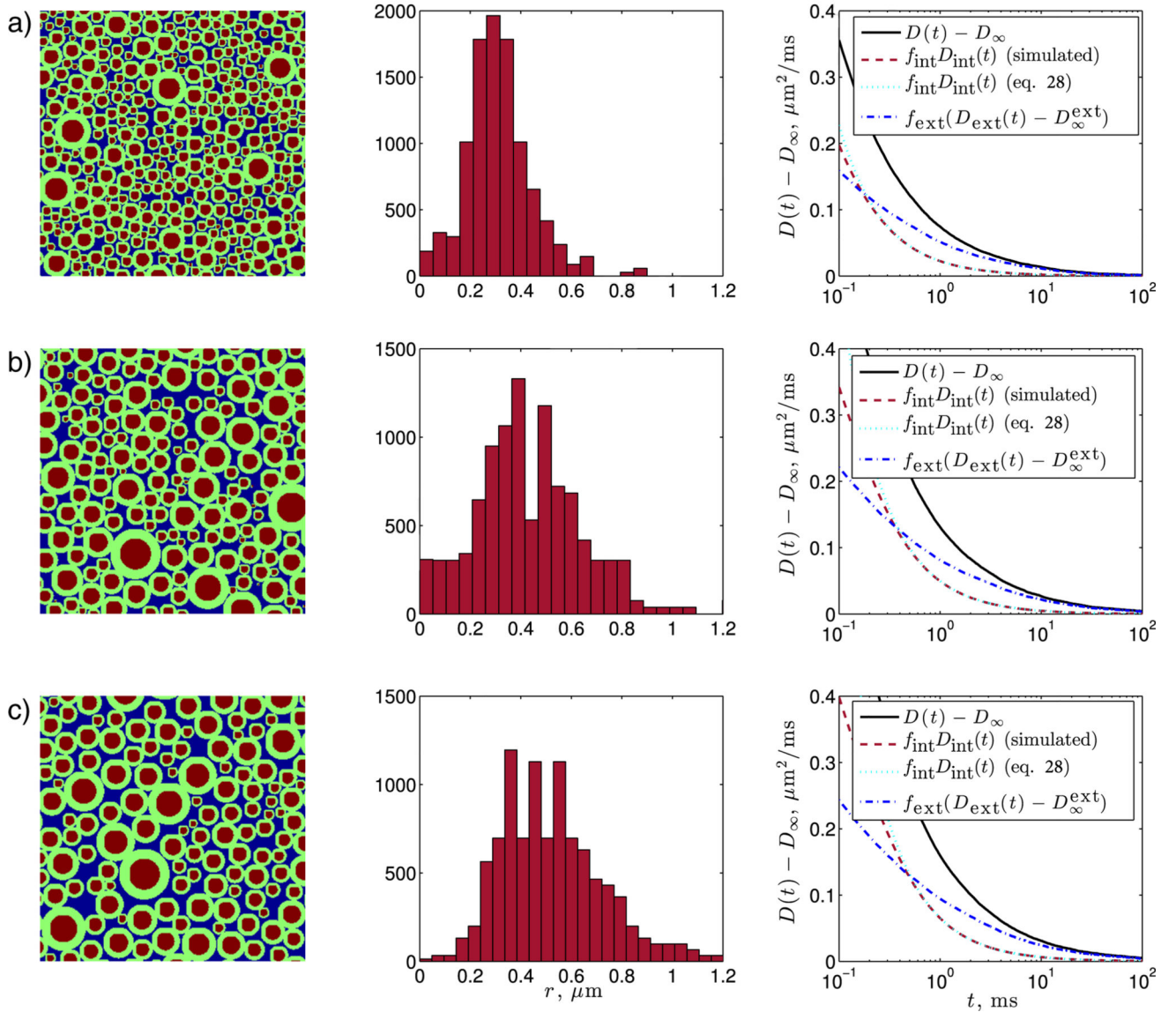
Fig. 11.
Simulated data for sectors 2, 4 and 6 (rows a, b and c) of the rhesus monkey corpus callosum based on data from Lamantia and Rakic (1990). Left column: Sample sections of the disk packs used in the MC simulation. For full packs, see Supplementary figs. S1–S3. Intra-axonal areas are indicated by the red pixels, with myelin and extra-axonal areas shown in green and blue, respectively. Center column: histograms of the internal radii used in each packing. Right column: the intra- and extra-axonal components of the long time diffusion coefficient. The total $D(t) - D_\infty$, Eq. (33), is given by the magenta solid line, the weighted intra-axonal component of the simulation, $f_{\text{int}}D_{\text{int}}(t)$, is given by the red dashed line, the weighted intraaxonal component calculated from Eq. (28) is given by the black dotted line, and the weighted extra-axonal component, $f_{\text{ext}}D_{\text{ext}}(t)$, from the Monte Carlo simulation (see Methods) is given by the blue dot dashed line.
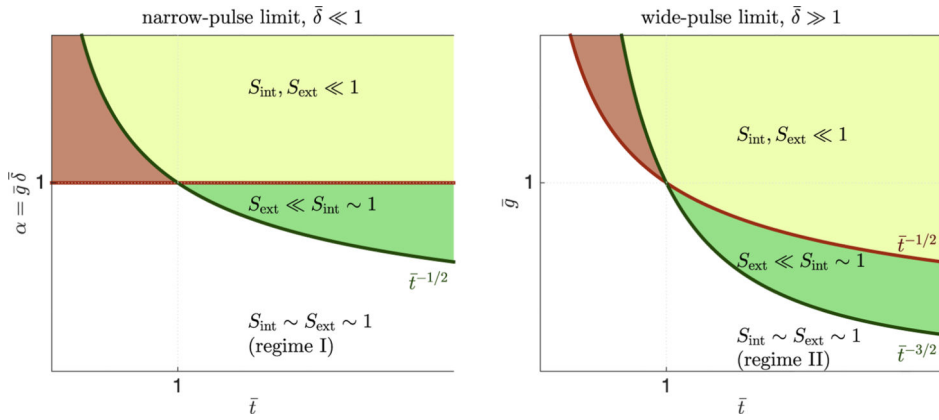
Fig. 12.

Phase diagram for dMRI transverse to axonal tract in the narrow-pulse and wide-pulse limits. In each panel, area above green line is where extra-axonal contribution is small, $S_{ext} \ll 1$, while area above red line is where intra-axonal contribution is small, $S_{int} \ll 1$. Green-shaded areas indicate applicability of ADM, i.e. sensitivity mostly to the intra-axonal contribution. Our results apply in the regime of weak gradients ($\bar{g} \sim 10^{-3}$ for clinical scanners), in which case both intra- and extra-axonal contributions are important, and ADM-measured axonal radii become strongly biased: regime I corresponds to Eq. (34) and regime II to Eq. (39).

Table 1

A summary of the long-time dependencies of the instantaneous diffusion coefficient, $D_{\text{inst}}(t)$, Eq. (4), PG-measured cumulative diffusion coefficient, $D(t)$, Eq. (3), and the OG-measured frequency-dependent diffusion coefficient, $D(\omega)$, Eq. (15), in 2d. Here $\tilde{t}_c$ is defined in Eq. (1).

Structure	$D_{\text{inst}}(t)$	PG: $D(t)$	OG: Re$D(\omega)$
Ordered (p = ∞), or confining	e^{-t/t_0}	$\dfrac{1}{t}$	ω^2
Short range disordered (p = 0)	$\dfrac{1}{t}$	$\dfrac{ln\left(t/\tilde{t}c\right)}{t}$	$|\omega|$

Table 2

Results from experiment, and from MC simulations in random disk packings for the geometries of the Dyneema phantom (Fig. 6b) and of sectors 2, 4, 6 of monkey CC (Fig. 11). The correlation length estimated as $l_c = \sqrt{4 D_\infty t_c}$ closely follows the mean external radius $\langle r_{ext} \rangle$ of the packings, while the amplitude A scales roughly with l_c^2, as l_c^2, cf. Supplementary fig. S4.

Parameter	Experiment	MC: phantom	Sector 2	Sector 4	Sector 6
D_0, μm^2/ms	1.8	1.8	2.0	2.0	2.0
D_∞ μm^2/ms	0.65	0.66	0.81	0.80	0.80
A, μm^2	7.41	5.56	0.046	0.117	0.126
$\tilde{t_c}$ or t_c, ms	13.90	13.76	0.132	0.319	0.276
t_c, μm	6.0	6.0	0.65	1.01	0.94
$\langle r_{ext} \rangle$, μm	8.5	8.5	0.53	0.73	0.88

Table 3

The relative contribution of the time-dependent part of $D_{\text{ext}}(t)$ in the time dependence of the total $D(t)$, and the corresponding overestimation of r_{app} compared to mean axon radius $<r>$, for $t = $ = 10 ms and 100 ms, cf. Fig. 2.

Ratio	Sector 2		Sector 4		Sector 6	
	10 ms	100 ms	10 ms	100 ms	10 ms	100 ms
$f_{\text{ext}}\left(D_{\text{ext}}(t) - D_{\infty}^{\text{ext}}\right) : D(t) - D_{\infty}$	0.84	0.85	0.82	0.89	0.79	0.88
$r_{\text{app}} :<r>, \delta = 0$	3.33	3.99	3.47	4.32	3.13	3.85
$r_{\text{app}} : <r>, \delta = 10$ ms	5.92	7.54	5.46	6.94	4.66	5.82